Responses to reviewer 1

Manuscript No.: SE-2019-8

Dear reviewer,

I appreciate for your second detailed reading and I am very glad that you have found revisions satisfactory. Thank you for your very positive and encouraging opinion about this study. Below I have made necessary correction for that single minor mistake you pointed out.

As in the first submission of revised version, I have highlighted the single change in red color in the main text.

Sincerely yours

Tuna Eken

Reviewer 1: On the revised manuscript titled "Moment magnitude estimates for Central Anatolian earthquakes using coda waves" by Tuna Eken, the Author sincerely responded to the Reviewer's comments. After correcting a very minor point (see below), this will be ready for the publication.

Text: L329: Add "(2018)" after "Malagnini and Munafò"

T.E.: This has been corrected as "Malagnini and Munafò (2018)" now.

Moment magnitude estimates for Central Anatolian earthquakes using coda waves

Tuna Eken[1]

[1]*Department of Geophysical Engineering, the Faculty of Mines, Istanbul Technical University, 34469 Maslak, Sarıyer, Istanbul, Turkey*

Abstract

Proper estimate of moment magnitude that is a physical measure of the energy released at earthquake source is essential for better seismic hazard assessments in tectonically active regions. Here a coda wave modeling approach that enables the source displacement spectrum modeling of examined event was used to estimate moment magnitude of central Anatolia earthquakes. To achieve this aim, three component waveforms of local earthquakes with magnitudes $2.0 \leq M_L \leq 5.2$ recorded at 72 seismic stations which have been operated between 2013 and 2015 within the framework of the CD-CAT passive seismic experiment. An inversion on the coda wave traces of each selected single event in our database was performed in five different frequency bands between 0.75 and 12 Hz. Our resultant moment magnitudes (M_W-coda) exhibit a good agreement with routinely reported local magnitude (M_L) estimates for study area. Apparent move-out that is, particularly, significant around the scattered variation of ML-MW-coda data points for small earthquakes (ML<3.5) can be explained by possible biases of wrong assumptions to account for anelastic attenuation and of seismic recordings with finite sampling interval. Finally, we present an empirical relation between M_W-coda and M_L for central Anatolian earthquakes.

Keyword(s): Coda waves modelling, seismic moment, moment magnitude, Radiative Transfer Theory

1. *Introduction*

The robust and stable knowledge of source properties (e.g. moment magnitude estimates) is crucial in seismically active countries such as Turkey for a better evaluation of seismic hazard potential as this highly depends on establishment of reliable seismicity catalogs. Moreover, accurate information on source parameters could be important when developing regional attenuation properties.

Conventional type of magnitude scales (M_L, m_b, M_S) as the result of empirically derived using direct wave analyses can be biased due to various effects such as source radiation pattern, directivity, and heterogeneities along the path since they may cause drastic changes in direct wave amplitude measurements (e.g., Favreau and Archuleta, 2003). Instead several early studies depending on the analysis of local and/or regional coda envelopes have indicated that coda wave amplitudes are significantly less variable by a factor of 3-to-5 compared to direct wave amplitudes (e.g., Mayeda and Walter, 1996; Mayeda et al., 2003; Eken et al., 2004; Malagnini et al., 2004; Gök et al., 2016). In fact local or regional coda waves that are usually considered to be generally to be composed of scattered waves and can be simply explained by that sample the single scattering model of Aki (1969) have been proven to be virtually insensitive to any source radiation pattern effect in contrast to direct waves because of the volume averaging property of the coda waves sampling the entire focal sphere (e.g., Aki and Chouet, 1975; Rautian and Khalturin, 1978). In Sato and Fehler (1998) and Sato et al. (2012) an extensive review study on the theoretical background of coda generation and advances of empirical observations and modelling efforts can be found in details.

There have been several approaches used for extracting information on earthquake source size via coda wave analyses. These approaches can be mainly divided into two groups. The first group of studies employs coda normalization strategy in which measurements require a correction for seismic attenuation parameters (e.g. intrinsic and scattering) that can be described by some empirical quality factors. To calibrate final source properties reference events are used to adjust measurements with respect to each other. For forward generation of synthetic coda envelopes, either single-backscattering or more advanced multiple-backscattering approximation are used. An example to this group is an empirical method originally developed by Mayeda et al. (2003) to investigate seismic source parameters such as energy, moment, and apparent stress drop in the western United States and in Middle East. They corrected observed coda envelopes for various influences, for instance, path effect, S-to-coda transfer function, site effect, and any distance-dependent changes in coda envelope shape. Empirical coda envelope method have been successfully applied to different regions with complicated tectonics such as northern Italy (e.g. Morasca et al., 2008), Turkey and Middle East (e.g. Eken et al., 2004; Gök et al. 2016); or Korean Peninsula (e.g. Yoo et al., 2013).

Second type of approach is a joint inversion technique that is based on a simultaneous optimization of source, path, and site specific terms via synthetic and observed coda envelope fitting within a selected time window including observed coda and direct-S wave parts. In this approach, the Radiative Transfer Theory (RTT) is employed for analytic expression of synthetic coda wave envelopes. The method that does not rely on coda normalization strategy was originally developed by Sens-Schönfelder and Wegler (2006) and successfully tested on local and regional earthquakes ($4 \leq Ml \leq 6$) detected by the German Regional Seismic Network. Further it has been applied to investigate source and frequency dependent

attenuation properties of different geological settings, i.e., Upper Rhine Graben and Molasse Basin regions in Germany and western Bohemia/Vogtland in Czechia (Eulenfeld and Wegler, 2016); entire United States (2017); central and western North Anatolian Fault Zone (Gaebler et al., 2018; Izgi et al., 2018). A more realistic earth model in which anisotropic scattering conditions were earlier considered by Gusev and Abubakirov (1987) yielded peak broadening effects of the direct seismic wave arrivals. This approach later was used in previous studies (e.g. Zeng, 1993; Przybilla and Korn, 2008; Gaebler et al., 2015) that dealt with propagation of P-wave elastic energy and the effect of conversion between P- and S-wave energies.

In the current work I present estimated source spectra as an output of a joint inversion of S- and coda waves parts of local earthquake waveforms 487 local earthquakes with magnitudes $2.0 < ML < 4.5$ detected in central Anatolia for their source parameters. The approach used here employs isotropic acoustic RTT approach for forward calculation of synthetic coda envelopes. Gaebler et al. (2015) has observed that modeling results from isotropic scattering were almost comparable with those inferred from relatively more complex elastic RTT simulations with anisotropic scattering conditions. The use of a joint inversion technique is advantageous since it is insensitive to any potential bias, which could be introduced by external information, i.e., source properties of a reference that is obtained separately from other methods for calibration. This is mainly because of the fact that we utilize an analytical expression of physical model involving source, and path related parameters to describe the scattering process. Moreover the type of optimization during joint inversion enables the estimates for source parameters of relatively small sized events compared to the one used in coda-normalization methods.

2. *Regional Setting and Data*

Present tectonic setting of Anatolia and surrounding regions have been mainly outcome of the northward converging movements among Africa, Arab, and Eurasian plates. To the west subducting African plate with a slab roll-back dynamics beneath Anatolia along Hellenic Trench has led to back-arc extension in the Aegean and western Anatolia while compressional deformation to the east around the Bitlis–Zagros suture was explained by collisional tectonics (e.g. Taymaz et al., 1990; Bozkurt, 2001) (Fig. 1). Central Anatolia is located between extensional regime to the west due to the subduction and compressional regime tectonics to the east due to the collisional tectonics. There are several fault systems responsible for ongoing seismic activity in the region. The major fault zone, the Central Anatolian Fault Zone (CAFZ) (Fig. 2), which primarily represents a transtensional fault structure with small amount of left-lateral offset during the Miocene (e.g. Koçyiğit and Beyhan, 1998), can be considered as a boundary between the carbonate nappes of the Anatolide-Tauride block from the highly deformed and metamorphosed rocks in the Kırşehir block. To the northwest of the CAFZ, Tuz Gölü Fault Zone (TGFZ) (Fig. 2), which is characterized by a right-lateral strike slip motion with a significant oblique-slip normal component, appears to be collocated with Tuz Gölü Basin sedimentary deposits as well as crystalline rocks within Kırşehir Block (e.g. Çemen et al., 1999; Bozkurt et al., 2001; Taymaz et al., 2004; Çubuk et al., 2014). At the southwest tip of the study region, the EAFZ generates large seismic activity that can be identified rather complicated seismotectonic setting: predominantly left-lateral strike-slip motion correlated well with the regional deformation pattern but also existing local clusters of thrust and normal faulting events on NS- and EW-trending subsidiary faults, respectively (Bulut et al., 2012). Such complicated behavior explains kinematic models of the shear deformation zone

126 evolution. It connects to the NAFZ at the Karlıova Triple Junction (Bozkurt, 2001) and to the
127 south splits into various segments nearby the Adana Basin (Kaymakci et al., 2006) (Fig. 2).
128 Toward the south, the EAFZ reaches the Dead Sea Fault Zone (DSFZ) that has a key role in
129 accommodating northward relative motions of Arabian and African Plates with respect to
130 Eurasia.
131
132 The present work utilizes three-component waveforms of local seismic activity detected at 72
133 broadband seismic stations (Fig. 2) that have been operated for 2 years between 2013 and
134 2015 within the framework of a temporary passive seismic experiment, the Continental
135 Dynamics–Central Anatolian Tectonics (CD-CAT) (Portner et al., 2018). We benefit from
136 revisited standard earthquake catalogue information (publicly available at
137 http://www.koeri.boun.edu.tr) to extract waveform data for a total of 2231 examined events
138 with station-event pair distance less than 120 km and focal depths less than 10 km. Most of
139 the detected seismic activity in the study area is associated to several fault zones in the region,
140 i.e., the EAFZ, CAFZ, DSFZ, TGFZ, etc. Here we note that selection of only local
141 earthquakes is to exclude possible biases, which may be introduced by Moho boundary
142 guided Sn-waves while upper crustal earthquakes are preferred in this study to exclude effect
143 of relatively large-scale heterogeneities on coda wave trains. Finally a visual inspection
144 conducted over all waveforms to ensure high-quality waveforms reduces our event number to
145 1193. Selected station and event distributions can be seen in Figure 2.
146
147 Observed waveforms were prepared at 5 different frequency bands with central frequencies at
148 0.75, 1.5, 3.0, 6.0, 12.0 Hz via a Butterworth band-pass filtering process. In the next step, we
149 applied Hilbert transform to filtered waveform data in order to obtain the total energy
150 envelopes. An average crustal velocity model was used to predict P and S wave onsets on

envelopes and then based on this information: (i) the noise level prior to the P-wave onset was eliminated (ii) S-wave window was determined starting at 3s prior to and 7 s afterwards S-wave onset as this allowed to include all direct S-wave energy, (iii) starting at the end of the S-wave window, a coda window of 100s at maximum was determined. Length of coda windows can be shorter when signal-to-noise ratio (SNR) is less than 2.5 or when the same window consists of coda waves from two earthquakes, which can give rise to a decline in the envelope. We omit the earthquakes with less than 10 s of coda length from our database.

3. Method

We adopted an inversion procedure that was originally developed by Sens-Schönfelder and Wegler (2006) and later modified by Eulenfeld and Wegler (2016). The forward part, which involves calculation of energy density for a specific frequency band caused by an isotropic source, is expressed in Sens-Schönfelder and Wegler (2006) as follows:

$$E_{mod}(t,r) = WR(r)G(t,r,g)e^{-bt} \qquad (1)$$

where W gives source term and it is frequency dependent. R(r) indicates the energy site amplification factor and b is intrinsic attenuation parameter. $G(t,r,g)$ represents Green's function that includes scattered wave field as well as direct wave and its expression is given by Paasschens (1997) as follows:

$$G(t,r,g) = e^{(-v_0 t g_0)}\left[\frac{\delta(r-v_0 t)}{4\pi r^2} + \left(\frac{4\pi v_0}{3g_0}\right)^{-\frac{3}{2}} t^{-\frac{3}{2}} \times \left(1-\frac{r^2}{{v_0}^2 t^2}\right)^{\frac{1}{8}} K\left(v_0 t g_0\left(1-\frac{r^2}{{v_0}^2 t^2}\right)^{\frac{3}{4}}\right) H(v_0 t - r)\right] \qquad (2)$$

Here the term within Dirac delta function represents direct wave and other term indicates

scattered waves. v_0 describes the mean S-wave velocity while g_0 is the scattering coefficient.

Possible discrepancy between predicted (Eq. 1) and observed energy densities for each event at each station with N_{ij} time samples (index k) in a specific frequency band can be minimized using:

$$\epsilon(g) = \sum_{i,j,k}^{N_S,N_S,N_{ij}} \left(lnE_{ijk}^{obs} - lnE_{ijk}^{mod}(g)\right)^2 \quad (3)$$

Here, the number of stations (index i) and events (index j) are shown by N_S and N_E, respectively. Optimization of g will be achieved when

$$lnE_{ijk}^{obs} = lnE_{ijk}^{mod} \qquad (4) \qquad \text{or}$$

$$lnE_{ijk}^{obs} = \ln Gt_{ijk}, r_{ijk}, g + lnR_i + lnW_j - bt_{ijk} \qquad (5)$$

Equation 5 simply define an overdetermined inversion problem with $\sum_{i,j} N_{ij}$ number equation systems and with $N_S + N_E + 1$ variables and thus b, R_i, and W_j can be solved via a least-squares technique. $\epsilon(g)$ can be defined as sum over the squared residuals of the solution.

Eulenfeld and Wegler (2016) present a simple recipe to perform inversion:

(i) Calculate Green's functions through the analytic approximation of the solution for 3-D isotropic radiative transfer (e.g. Paasschens 1997; Sens-Schönfelder and Wegler, 2006) by using fixed scattering parameters and minimize equation 5 to solve for b, R_i, and W_j via a weighted least-squares approach.

(ii) Calculate $\epsilon(g)$ using equation 3.

195 (iii) Repeat (i) and (ii) by selecting different g to find the optimal parameters g, b, R_i and W_j
196 that finally minimize the error function ϵ.

197 In Fig. 3 an example for the minimization process that was applied at five different frequency
198 bands is displayed for one selected event at recorded stations of the CD-CAT project.

199 Minimization described above for different frequencies will yield unknown spectral source
200 energy term, W_j as well as site response, R_i and attenuation parameters, b, and g that will
201 satisfy optimal fitting between observed and predicted coda wave envelopes. Example for this
202 fitting can be seen in Figure 4. The present study deals with frequency dependency of W_j
203 since this information can be later useful to obtain source displacement spectrum and thus
204 seismic moment and moment magnitudes of analyzed earthquakes using the formula of the *S*-
205 wave source displacement spectrum for a double-couple source in the far-field, which is given
206 by Sato et al. (2012):

207 $$\omega M(f) = \sqrt{\frac{5\rho_0 v_0^5 W}{2\pi f^2}} \quad (6)$$

208

209 The relation between the obtained source displacement spectrum and seismic moment value
210 was earlier described in Abercrombie (1995) by:

211 $$\omega M(f) = M_0 \left(1 + \left(\frac{f}{f_c}\right)^{\gamma n}\right)^{-\frac{1}{\gamma}} \quad (7)$$

212 where n is related to the high-frequency fall-off and γ is known as shape parameter that
213 controls the sharpness of spectrum at corner frequency between the constant level M_0 (low
214 frequency part) and the fall-off with f^{-n} (high frequency part). Taking logarithm of equation 7
215 gives:

$$\ln \omega M(f) = lnM_0 - \frac{1}{\gamma}\ln\left(1 + \left(\frac{f}{f_c}\right)^{\gamma c}\right) \quad (8)$$

Eq. 8 describes an optimization problem of which data forms observed source displacement spectrum and four source parameters, M_0, γ, n, and f_c are the unknown model parameters that can be resolved in a simultaneous least-squares inversion of the equation 8. Finally moment magnitude, M_W can be calculated from modeled source parameters, seismic moment, M_0 using a formula given by Hanks and Kanamori (1979):

$$M_w = \frac{2}{3} log_{10} M_0 - 6.07 \quad (9)$$

4. Results and Discussions

4.1 Coda wave source spectra

Figure 5 displays observed values of source spectra established by inserting inverted spectral source energy term W at each frequency in Eq. 6 for all analyzed events. Each curve in this figure represents model spectrum estimate based on inversion procedure described in previous section. Modeled spectrum characteristics computed for 487 local earthquakes of which lateral distribution is presented in Figure 2 suggest, in general, that we were able to obtain typically expected source displacement spectrum with a flat region around the low frequency limit and decaying behaviour above a corner frequency.

Owing to the multiple-scattering process within small scale heterogeneities that makes coda waves gain an averaging nature, the variation in coda amplitudes due to differences source radiation pattern and path effect are reduced (Walter et al., 1995; Mayeda et al., 2003). Eulenfeld and Wegler (2016) found that radiation pattern would have only a minor influence

241 on the S-wave coda while it might disturb attenuation models inferred from the direct S-wave
242 analyses unless the station distribution relative to the earthquakes indicates a good azimuthal
243 coverage. A peak-like source function assumption for small earthquakes that are utilized in
244 the present work was earlier proven to be adequate in early application of the coda-wave
245 fitting studies (e.g. Sens-Schönfelder and Wegler, 2006; Gaebler et al., 2015; and Eulenfeld
246 and Wegler, 2016).
247
248 Conventional approaches (e.g. Abercrombie, 1995; Kwiatek et al., 2011) to estimate source
249 parameters such as corner frequency, seismic moment, high-frequency fall-off through fitting
250 of observed displacement spectra observed at a given station in an inversion scheme could be
251 misleading since these methods usually: (i) assume a constant value of attenuation effect (no
252 frequency variation) defined by a factor exp ($-\pi ftQ^{-1}$) over the spectrum, (ii) and assume
253 omega-square model with a constant high-frequency fall-off parameter, n=2. Following Sens-
254 Schönfelder and Wegler (2006) and Eulenfeld and Wegler (2016), however, we estimate
255 attenuation parameters (intrinsic and scattering) seperately within a simultaneous inversion
256 procedure in which high-frequency fall-off parameter varies. This is fairly consistent with
257 early studies (e.g. Ambeh and Fairhead, 1991; Eulenfeld and Wegler, 2016) where significant
258 deviations from the omega square model (n>3) were reported implying that the omega-square
259 model as a source model for small earthquakes must be reconsidered in its general
260 acceptance. Earlier it has been well-observed that the source spectra, especially, for large
261 earthquakes could be better explained by models of two corner frequencies (e.g.,
262 Papageorgiou and Aki, 1983; Joyner, 1984; Atkinson, 1990). Recently, Denolle et al. (2016)
263 observed that conventional spectral model of a single-corner frequency and high-frequency
264 fall-off rate could not explain P wave source spectra of thrust earthquakes with magnitude
265 Mw 5.5 and above. Instead, they suggested the double-corner-frequency model for large

266 global thrust earthquakes with a lower corner frequency related to source duration and with an
267 upper corner frequency suggesting a shorter time scale unrelated to source duration, which
268 exhibits its own scaling relation. Uchide and Imanishi (2016) reported similar differences
269 from the omega-square model would be valid also for smaller earthquakes by using spectral
270 ratio technique that involves empirical Green's function (EGF) events to avoid having a
271 complete knowledge of path and site effects for shallow target earthquakes (M_W 3.2–4.0) in
272 Japan. The source spectra for many of the target events in their study suggested a remarkable
273 discrepancy from the omega-square model for relatively small earthquakes. They explained
274 such differences by incoherent rupture due to heterogeneities in fault properties and applied
275 stress, the double-corner-frequency model, and possibility of a high-frequency falloff
276 exponent value slightly higher than 2. In our case, the smallest event was with M_W-coda
277 larger than 2.0, thus we had no chance to make a similar comparison, however, high-
278 frequency fall-off parameters varied from n=0.5 to n=4. A notable observation in the
279 distribution of n was n=2 or n=2.5 would be better explained for earthquakes with M_W-coda
280 >4.0 whereas the smaller magnitudes exhibited more scattered pattern of variation in n
281 (Figure 7). Eulenfeld and Wegler (2016) claimed that the use of separate estimates of the
282 attenuation or correction for path effect via emprically determined Green's function would be
283 better strategy in order to invert station displacement spectra for source parameters. This is
284 mainly because smaller earthquakes (with n>2), in particular, assuming omega-square model
285 can distort the estimates of corner frequency and even seismic moment especially in regions
286 where Q is strongly frequency dependent.
287
288 *4.2 Coda wave –derived magnitude vs. M_L catalogue magnitude*
289 A scatter plot between catalogue magnitudes based on local magnitudes (M_L) and our coda-
290 derived magnitudes (M_W-coda) that are inferred from resultant frequency dependent source

displacement spectra and thus seismic moment (e.g. Eq. 9) is shown in Fig. 6. Such comparison suggests an overall coherency between both types of magnitudes. This implies very simple model of a first-order approximation for S-wave scattering with isotropic acoustic radiative transfer approach can be efficient to link the amplitude and decaying character of coda wave envelopes to the seismic moment of the source.

In the present study, a linear regression analyses performed between M_W-coda and M_L magnitudes (Fig. 5) resulted in an emprical formula that can be employed to convert local magnitudes into coda-derived moment magnitude calculation of local earthquakes in this region:

$$M_{W-coda} = 1.1655 \pm 0.0337 \times M_L - 0.7085 \pm 0.0128 \quad (10)$$

Bakun and Lindh (1977) empirically described the linear log seismic moment-local magnitude relation between seismic moments (Mo) and local magnitudes (M_L) for earthquakes near Oroville, California. Beside this several other studies investigated to find an optimum relation between M_W and M_L by implementing linear and/or non-linear curve-fitting approaches. Malagnini and Munafò (2018) proposed two different linear fits separated by a crossover M_L=4.31 could represent M_L-M_W data points obtained from earthquakes of the central and northern Apennines, Italy. Several coefficient of regression analyses in their fits account for the combined effects of source scaling and crustal attenuation as well as regional attenuation, focal depth, and rigidity at source. Goertz-Allmann et al. (2011), for instance, introduced hybrid type of scaling relation that is linear below M_L 2 and above M_L 4 and a quadratic relation in between ($2 \leq M_L \leq 4$) for earthquakes in Switzerland detected between 1998 and 2009. Edwards and Rietbrock (2009) employed a second-order polynomial equation

316 to relate local magnitudes routinely reported in the Japan Meteorological Agency (JMA)
317 magnitude and moment magnitude. More recently, using multiple spectral ratio analyses
318 Uchide and Imanishi (2018) estimated relative moment magnitudes for the Fukushima
319 Hamadori and the northern Ibaraki prefecture areas of Japan and reported a quadratic form of
320 correlation between JMA magnitudes and moment magnitudes. Resultant empirical curve in
321 Uchide and Imanishi (2018) implied a considerable discrepancy between the moment
322 magnitudes and the JMA magnitudes, with a slope of 1/2 for microearthquakes suggesting
323 possible biases introduced by anelastic attenuation and the recording by a finite sampling
324 interval.
325
326 Apparent move-out in Fig. 5 and Eq. 10, presumably stems from the use of different
327 magnitude scales for comparison. Conventional magnitudes scales such as M_L, mb inferred
328 from phase amplitude measurements are seemingly sensitive to attenuation and 2D variation
329 along the path (Pasyanos et al., 2016). Unlike local magnitude scales, seismic moment-based
330 moment magnitude (M_W) essentially represents a direct measure of the strength of an
331 earthquake caused by fault slip and is estimated from relatively flat portion of source spectra
332 at lower frequencies that can be less sensitive to the near surface attenuation effects. The
333 consistency between coda-derived moment magnitude and local magnitude scales for the
334 earthquakes with M_W-coda > 3.0 indicates that our non-empirical approach successfully
335 worked in this tectonically complex region. This observation is anticipated, for relatively
336 large earthquakes, since more energy will be characteristic at lower frequencies. We
337 observed similar type of consistency in early studies that investigate source properties of local
338 and regional earthquakes based on emprical coda methods with simple 1-D radially
339 symmetric path correction (e.g. Eken et al., 2004; Gök et al., 2016). Coda waves–derived
340 source parameters were obtained with high-precision in Mayeda et al. (2005), Phillips et al.

(2014), Pasyanos et al. (2016) following the use of 2-D path-corrected station techniques to consider the amplitude-distance relationships. Observable outliers in Figure 5, for the events with less than Mw 3.5, however, can be attributed to the either possible biases on local magnitude values taken from the catalogue or small biases on our intrinsic (Q_i^{-1}) and scattering (Q_s^{-1}) attenuation terms. One another possible contribution to such mismatch might be associated to the influences of mode conversions between body and surface waves or surface-to-surface wave scattering (e.g. Wu & Aki 1985) that are not restricted to low frequencies (<1Hz) (Sens-Schönfelder and Wegler, 2006).

5. Conclusions

This study provides an independent solution for estimating seismic source parameters such as seismic moment and moment magnitude for local earthquakes in central Anatolia without requiring *a priori* information on reference events with waveform modelling results to be used for calibration or *a priori* information on attenuation for path effect corrections. In this regard, the approach used here can be easy and useful tool for investigation of source properties of local events detected at temporal seismic networks. Moreover, seismic moment can be approximated via waveform modelling methods but due to the small-scale heterogeneities of the media that waves propagate, it is often a hard task to establish Green's function for small earthquakes (M_L < 3.5). An analytical expression of energy density Green's function in a statistical manner employed in the present work enables neglecting the interaction of the small-scale inhomogeneities with seismic waves as this can be practical for seismic moment calculations of small events that may pose source energy at high-frequency. It is noteworthy to mention that our isotropic scattering assumption does not consider anisotropic case, which could be valid for real media, but still provides a simple and effective tool to define the transport for the anisotropic case since the estimated scattering coefficient

can be interpreted as transport scattering coefficient. An averaging over S-wave window enables to overcome biases caused by using unrealistic Green's function (Gaebler *et al.* 2015). Since the present study mainly focuses on source properties of local earthquakes in the study area, scattering and intrinsic attenuation properties that are other products of our coda envelope fitting procedure will be examined in details within a future work. Finally, the empirical relation developed between M_W-coda and M_L will be a useful tool for quickly converting catalogue magnitudes to moment magnitudes for local earthqukes in the study area.

Data and resources

The python code used for carrying out the inverse modeling is available under the permissive MIT license and is distributed at https://github.com/trichter/qopen. We are grateful to the IRIS Data Management Center for maintaining, archiving and making the continuous broadband data used in this study open to the international scientific community.

Acknowledgement

The facilities of IRIS Data Services, and specifically the IRIS Data Management Center, were used for access to waveforms, related metadata, and/or derived products used in this study. IRIS Data Services are funded through the Seismological Facilities for the Advancement of Geoscience and EarthScope (SAGE) Proposal of the National Science Foundation under Cooperative Agreement EAR-1261681. Data for the CD-CAT experiment (https://doi.org/10.7914/SN/YB_2013) are available from the IRIS Data Management Center at http://www.iris.edu/hq/. Tuna Eken acknowledge financial support from Alexander von Humboldt Foundation (AvH) towards computational and peripherals resources. I am grateful to the Topical Editor Charlotte Krawczyk for handling the revision process and Takahiko

391 Uchide for his valuable opinions on the improvement of manuscript.

392 *References*

393 Abercrombie, R.E.: Earthquake source scaling relationships from −1 to 5 ML using
394 seismograms recorded at 2.5-km depth, J. geophys. Res., 100(B12), 24 015–24 036,
395 1995.
396 Aki, K., and Chouet., B.: Origin of coda waves: Source, attenuation, and scattering effects, J.
397 Geophys. Res. 80, 3322–3342, 1975.
398 Atkinson, G. M.: A comparison of eastern North American ground motion observations with
399 theoretical predictions, Seismol. Res. Lett. 61, 171–180, 1990.
400 Bakun, W.H. and Lindh, A.G.: Local Magnitudes, Seismic Moments, and Coda Durations for
401 Earthquakes Near Oroville, California, Bulletin of the
402 SeismologicalSocietyofAmerica.Vol.67,No.3, pp. 615-629, 1977.
403 Bozkurt, E.: Neotectonics of Turkey—A synthesis: Geodinamica Acta, v. 14, p. 3–30, 2001.
404 Bulut, F., Bohnhoff, M., Eken, T., Janssen, C., Kılıç, T., and Dresen, G.: The East Anatolian
405 fault zone: Seismotectonic setting and spatiotemporal characteristics of seismicity based
406 on precise earthquake locations: Journal of Geophysical Research, v. 117, B07304,
407 https://doi .org/10.1029/2011JB008966, 2012.
408 Çemen, I., Göncüoglu, M.C., and Dirik, K.: Structural evolution of the Tuz Gölü basin in central
409 Anatolia, Turkey: Journal of Geology, v. 107, p. 693–706, https://doi.org/10.1086
410 /314379, 1999.
411 Çubuk Y, Yolsal-Çevikbilen S, Taymaz, T.: Source parameters of the 20052008 Balˆa Sirapinar
412 (central Turkey) earthquakes: Implications for the internal deformation of the Anatolian
413 plate. Tectonophysics 635(Supplement C) :125 – 153, 2014.
414 Denolle, M. A., and Shearer, P.M.: New perspectives on self-similarity for shallow thrust
415 earthquakes, *J. Geophys. Res. Solid Earth*, *121*, 6533–6565, 2016.

416 Edwards, B., & Rietbrock, A.: A comparative study on attenuation and source-scaling relations
417 in the Kantō, Tokai, and Chubu regions of Japan, using data from Hi-net and KiK-net.
418 Bulletin of the Seismological Society of America, 99, 2435–2460, 2009.

419 Eken, T., Mayeda, K., Hofstetter, A., Gök, R., Orgülü, G. and Turkelli, N.: An application of the
420 coda methodology for moment-rate spectra using broadband stations in Turkey.
421 Geophys. Res. Lett, 31, L11609, 2004.

422 Eulenfeld, T. and Wegler, U.: Measurement of intrinsic and scattering attenuation of shear
423 waves in two sedimentary basins and comparison to crystalline sites in Germany,
424 Geophys J Int., 205(2):744-757, 2016.

425 Eulenfeld, T. and Wegler, U.: Crustal intrinsic and scattering attenuation of high-frequency
426 shear waves in the contiguous United States. J Geophys., Res, 122, 2017.

427 Favreau, P., and Archuleta, R.J.: Direct seismic energy modelling and application to the 1979
428 Imperial Valley earthquake, Geophys. Res. Lett., 30, 1198, 2003.

429 Gaebler, P.J., Eulenfeld, T. & Wegler, U.: Seismic scattering and absorption parameters in the
430 W-Bohemia/Vogtland region from elastic and acoustic radiative transfer theory,
431 Geophys. J. Int., 203(3), 1471–1481, 2015.

432 Gaebler, P.J., Eken, T., Bektaş, H.Ö, Eulenfeld, T., Wegler, U., Taymaz, T.: Imaging of Shear
433 Wave Attenuation Along the Central Part of the North Anatolian Fault Zone, Turkey,
434 submitted to the Journal of Seismology, 2018.

435 Goertz-Allmann, B. P., Edwards, B., Bethmann, F., Deichmann, N., Clinton, J., Fäh, D., &
436 Giardini, D.: A new empirical magnitude scaling relation for Switzerland. Bulletin of the
437 Seismological Society of America, 101, 3088–3095, 2011.

438 Gök, R., Kaviani, A., Matzel, E. M., Pasyanos, M. E., Mayeda, K., Yetirmishli, G., El-Hussain,
439 I., Al-Amri, A., Al-Jeri, F., Godoladze, T., Kalafat, D., Sandvol, E. A., and Walter,

440 W.R.: Moment Magnitudes of Local/Regional Events from 1D Coda Calibrations in the
441 Broader Middle East Region. Bull Seismol Soc Am., 106(5):1926-1938, 2016.
442 Gusev, A.A. & Abubakirov, I.R.: Simulated envelopes of non-isotropically scattered body
443 waves as compared to observed ones: another manifestation of fractal heterogeneity,
444 Geophys. J. Int., 127(1), 49–60, 1996.
445 Hanks, T.C. and Kanamori, H.: A moment magnitude scale, J. Geophys., Res., 84, 2348–2350,
446 1979.
447 Izgi, G., Eken, T., Gaebler, P., and Taymaz, T.: Frequency-Dependent Shear Wave Attenuation
448 Along the Western Part of the North Anatolian Fault Zone, Geophysical Research
449 Abstracts, Vol. 20, EGU2018-629-2, 2018.
450 Kaymakci, N. Inceöz, M. Ertepinar, P.: 3D architecture and Neogene evolution of the Malatya
451 Basin: inferences for the kinematics of the Malatya and Ovacik Fault Zones. Turkish
452 Journal of Earth Sciences, 15, 123-154, 2006.
453 Kwiatek, G., Plenkers, K. & Dresen, G.: 2011. Source parameters of pico-seismicity recorded at
454 Mponeng Deep Gold Mine, South Africa: implications for scaling relations, Bull. seism.
455 Soc. Am., 101(6), 2592–2608, 2011.
456 Malagnini, L., Mayeda, K., Akinci, A., and Bragato, P. L.: Estimating absolute site effects,
457 Bull. Seismol. Soc. Am. 94, no. 4, 1343–1352, 2004.
458 Malagnini, L., and Munafò., I.: On the Relationship between M_L and Mw in a Broad Range: An
459 Example from the Apennines, Italy, Bulletin of the Seismological Society of America,
460 Vol. 108, No. 2, pp. 1018–1024, 2018.
461 Mayeda, K., and Walter, W.R.: Moment, energy, stress drop, and source spectra of western
462 United States earthquakes from regional coda envelopes, J. Geophys. Res. 101, 11,195–
463 11,208, 1996.

464 Mayeda, K., Hofstetter, A., O'Boyle, J.L., and Walter, W.R.: Stable and transportable regional
465 magnitudes based on coda-derived moment-rate spectra, Bull. Seismol. Soc. Am. 93,
466 224–239: 2003.

467 Mayeda, K., Malagnini, L., Phillips, W. S., Walter, W. R., and Dreger, D.: 2D or not 2D, that is
468 the question: A Northern California Test. Geophys- ical Research Letters, 32(12), 2005.

469 Morasca, P., Mayeda, K., Malagnini, L. and Walter,W.R.: Coda and direct-wave attenuation
470 tomography in northern Italy, Bull Seismol Soc Am., v. 98, pages, 1936-1946, 2004.
471 Morasca, P., Mayeda, K., Gök, R., Phillips, W.S., and Malagnini, L.: Coda-derived source
472 spectra, moment magnitudes and energy-moment scaling in the western Alps, Geophys.
473 J. Int., 160, 263–275, 2008.
474 Paasschens, J.: Solution of the time-dependent Boltzmann equation, Phys. Rev. E, 56(1), 1135–
475 1141, 1997.
476 Papageorgiou, A., and Aki, K.: A specific barrier model for the quantitative description of
477 inhomogeneous faulting and the prediction of strong ground motion I: Description of the
478 model, Bull. Seismol. Soc. Am., 73(3), 693–722, 1983.
479 Pasyanos, M. E., R. Gök, and Walter, W.R.: 2-D variations in coda amplitudes in the Middle
480 East. Bull. Seismol. Soc. Am. 106, no. 5, 2016.
481 Phillips, W. S., Mayeda, K. M., and Malagnini, L.: How to invert multi-band, regional phase
482 amplitudes for 2-d attenuation and source parameters: Tests using the usarray. Pure and
483 Applied Geophysics, 171(3):469-484, 2014.
484 Portner, D.E., Delph, J.R., Biryol, C.B., Beck, S.L., Zandt, G., Özacar, A.A., Sandvol, E., and
485 Türkelli, N.: Subduction termination through progressive slab deformation across
486 Eastern Mediterranean subduction zones from updated P-wave tomography beneath
487 Anatolia, Geosphere, 14(3): 907-925, 2018.

Przybilla, J. and Korn, M.: Monte Carlo simulation of radiative energy transfer in continuous elastic random mediathree-component envelopes and numerical validation. Geophys J Int , 173(2):566-576, 2008.

Rautian, T.G. & Khalturin, V.I.: The use of the coda for determination of the earthquake source spectrum, Bull. Seism. Soc. Am., 68(4), 923–948, 1978.

Sato, H. and Fehler, M.C.: Seismic Wave Propagation and Scattering in the Heterogeneous Earth, Springer-Verlag, New York, 1998.

Sato, H., Fehler, M.C. & Maeda, T. Seismic Wave Propagation, and Scattering in the Heterogeneous Earth, 2nd edn, Springer: 2012.

Sens-Schönfelder, C. and Wegler, U.: Radiative transfer theory for estimation of the seismic moment. Geophys J Int, 167(3):1363-1372.

Taymaz, T., Jackson, J., Westaway, R.: Earthquake mechanisms in the Hellenic Trench near Crete. Geophys. J. Int.102, 695–731, 1990.

Taymaz, T., Westaway, R., Reilinger, R.: Active faulting and crustal deformation in the eastern Mediterranean Region. Spec. Issue Tectonophys. 391 (1-4), 1–9. http:// dx.doi.org/10.1016/j.tecto.2004.07.005, 2004.

Uchide, T., & Imanishi, K.: Small earthquakes deviate from the omega-square model as revealed by multiple spectral ratio analysis. Bulletin of the Seismological Society of America, 106(3), 1357–1363, 2016.

Uchide, T., & Imanishi, K.: Underestimation of microearthquake size by the magnitude scale of the Japan Meteorological Agency: Influence on earthquake statistics. Journal of Geophysical Research: Solid Earth, 123, 606–620, 2018.

Yoo, S.-H., Rhie, J., Choi, H.-S., and Mayeda, K.: Coda-derived source parameters of earthquakes and their scaling relationships in the Korean Peninsula, Bull. Seismol. Soc. Am., 101, 2388–2398, 2011.

513 Wu, R. and Aki, K.: The fractal nature of the inhomogeneities in the lithosphere evidenced from
514 seismic wave scattering, Pure appl. Geophys., 123(6), 805–818, 1985.
515 Zeng, Y., Su, F. and Aki, K.: Scattering wave energy propagation in a random isotropic
516 scattering medium: 1. Theory, J. Geophys. Res., 96(B1), 607–619, 1991.
517

518 *Figure Captions*

519 Figure 1. Major tectonic features of Turkey and its adjacent. The plate boundary data used
520 here is taken from Bird (2003). Subduction zones are black, continental transform faults are
521 red, continental rift boundaries are green, and spreading ridges boundaries are yellow. NAFZ,
522 EAFZ, and DSFZ are the North Anatolian Fault, East Anatolian Fault, and the Dead Sea fault,
523 respectively.
524

525 Figure 2. Epicentral distribution of all local events selected from the study area in the KOERI
526 catalogue. Gray circles represent earthquakes with poor quality that are not considered for the
527 current study while black indicates the location of local events with good quality. Red circles
528 among these events are 487 events used in coda wave inversion since they are successful at
529 passing quality criteria of further pre-processing procedure.
530

531 Figure 3. An example from the inversion procedure explained in chapter 3. Here coda
532 envelope fitting optimization is performed on band-pass filtered (8-16Hz) digital recordings
533 of an earthquake (2014 April 09, M_W-coda3.2) extracted for 7 seismic stations that operated
534 within the CD-CAT array. Large panel at the lower left-hand side displays the error function ε
535 as a function of g_0. Thick blue cross here represent the optimal value of $g = g_0$. Other small
536 panels at upper and right-hand side show the least- squares solution of the weighted linear
537 equation system for the first 6 guesses and optimal guess for g_0. There dots and gray curves

indicate the ratio between energy (E^{obs}) and the Green's function (G) obtained for direct S-waves and observed envelopes at various stations, respectively. Please notice that during this optimization process envelopes are corrected for the obtained site corrections R_i. The slope of linear curve at each small panel yields −b and while its intercept W are the intrinsic attenuation and source related terms at the right-hand side of equation 5 part of the right-hand side of the equation system.

Figure 4. a) Results of the inversion of the 2014-April-09, M_W-coda3.2 earthquake: Sample fits between observed and calculated energy densities in the frequency band 0.5–1.0 Hz are given for 6 different stations (see upper right corner for event ID, station name, and distance to hypocenter). Note that light blue curves represent observed envelope. Smoothed observed calculated envelopes in each panel are presented by blue and red curves, respectively. Blue and red dots exhibit location of the average value for observed and calculated envelopes within the S-wave window, respectively. b) The same as in (a) obtained in the frequency band 4.0–8.0 Hz.

Figure 5. All individual observed (black squares) and predicted (gray curve) source displacement spectra observed at 72 stations from 487 local earthquakes in central Anatolia.

Figure 6: Scatter plot between local magnitudes (M_L) of analyzed events with coda waves-derived magnitudes (M_W-coda) of the same events. The outcome of a linear regresssion analysis yielded an emprical formula (e.g. Eq. ~~9~~10) to identify the overall agreement represented by gray straight line. Yellow and red dashed lines indicate upper and lower limit of linearly fitting to that scatter.

Figure 7: Same scatter plot displayed in Fig. 6 color coded by estimated high-frequency fall-off parameter for each inverted event.

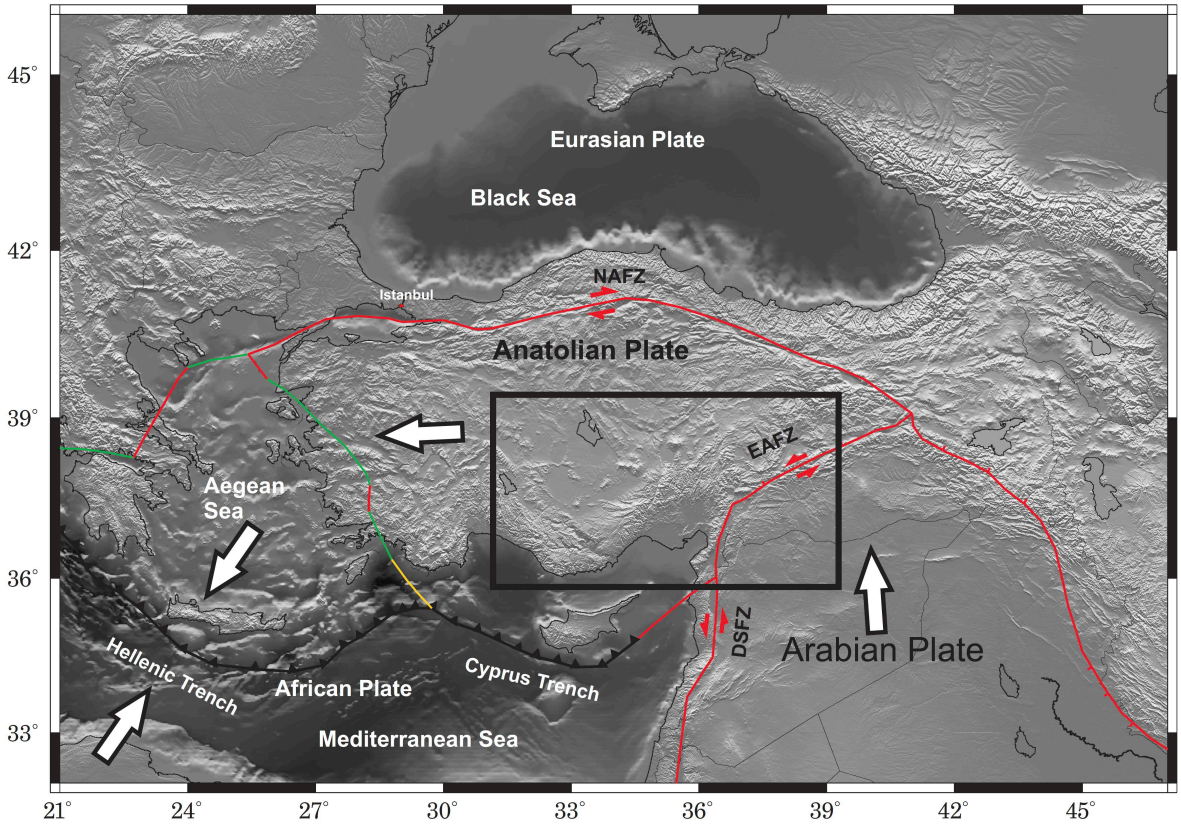

Figure 1.

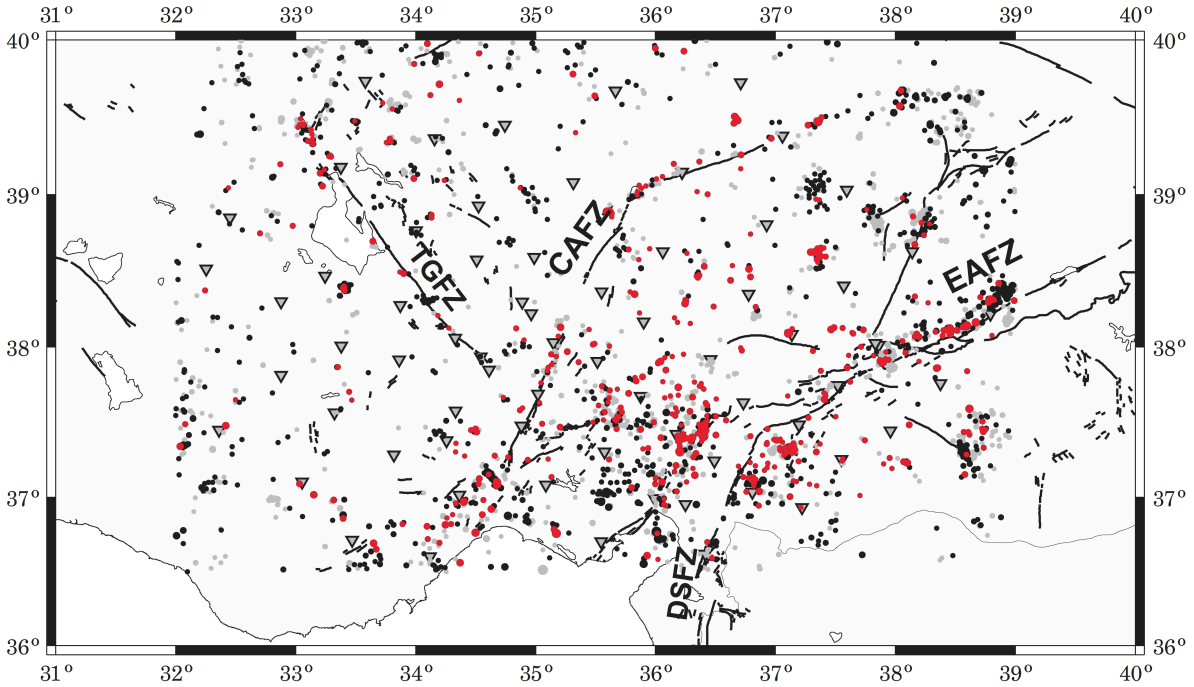

Figure 2.

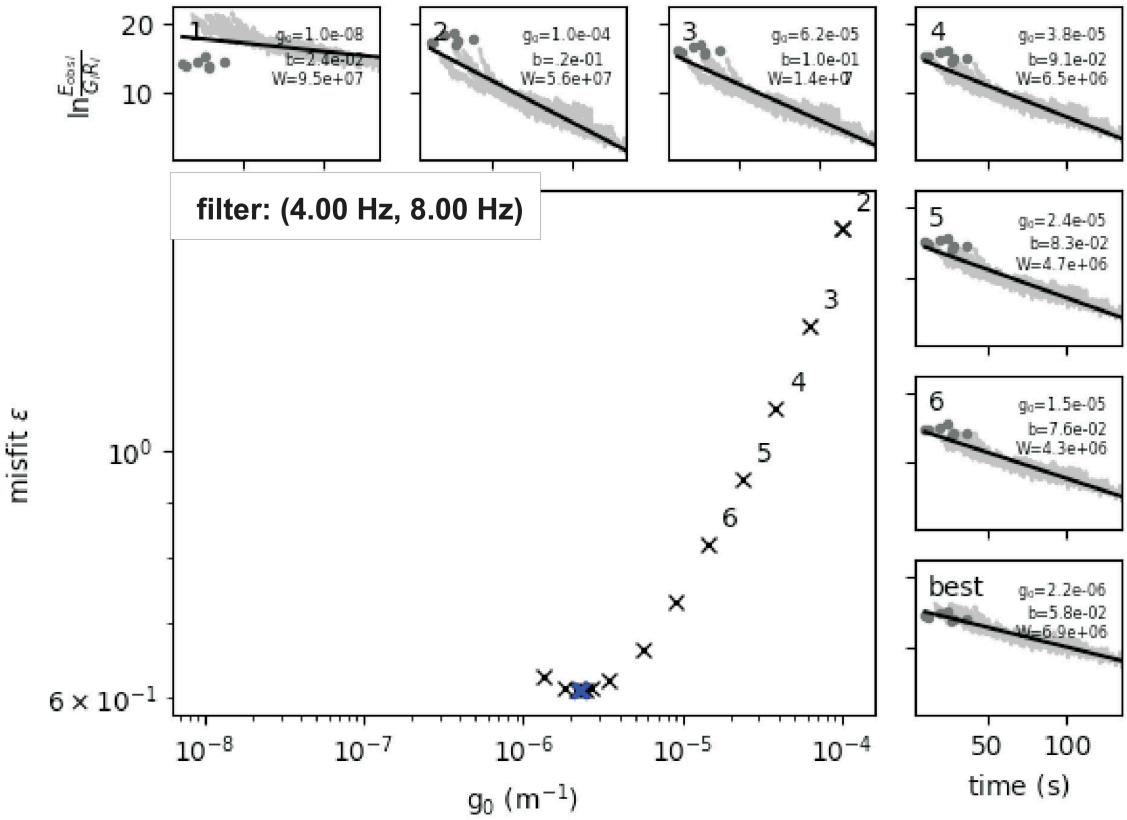

Figure 3.

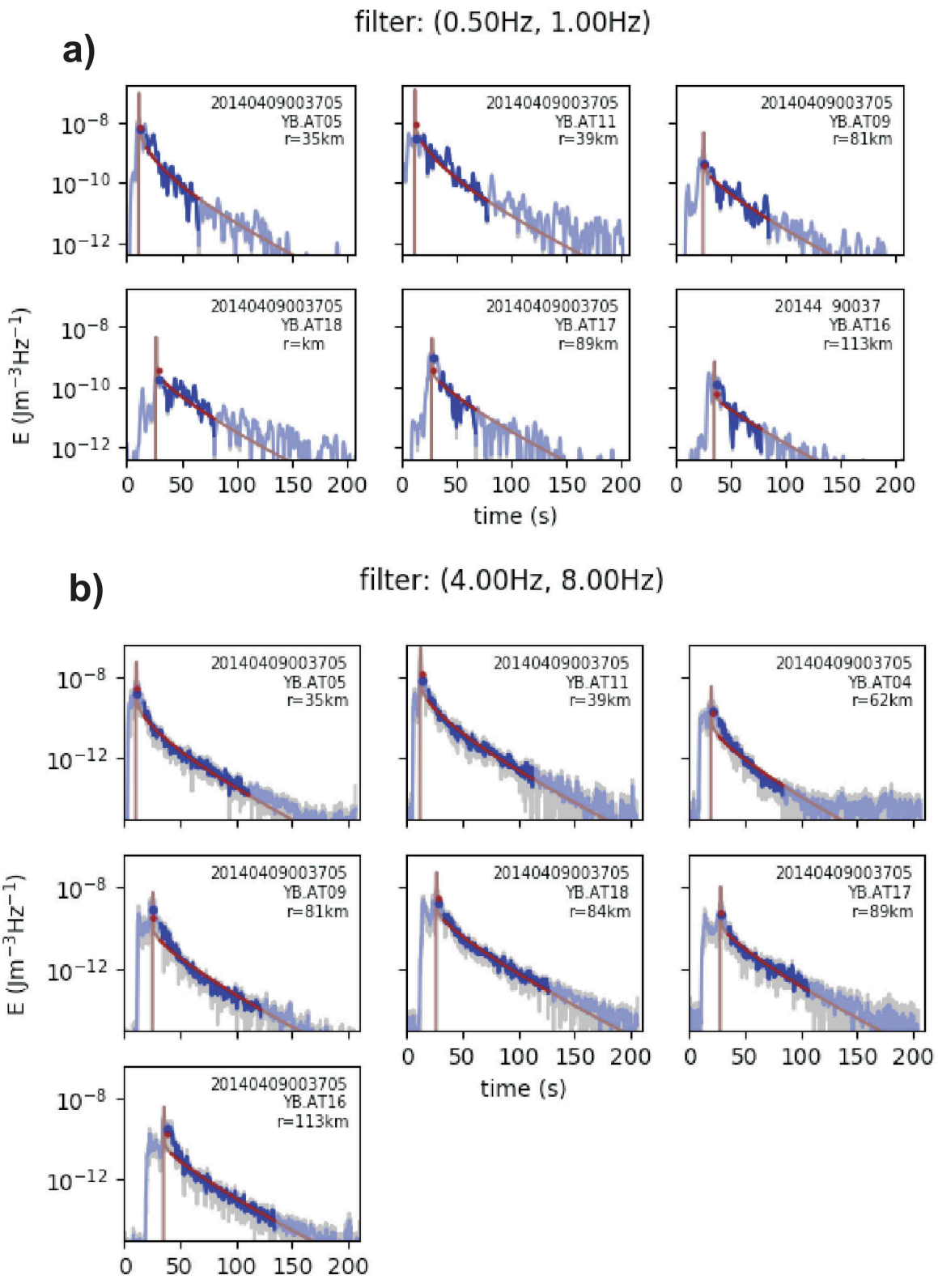
a)
filter: (0.50Hz, 1.00Hz)
20140409003705
YB.AT05
r=35km
20140409003705
YB.AT11
r=39km
20140409003705
YB.AT09
r=81km
20140409003705
YB.AT18
r=km
20140409003705
YB.AT17
r=89km
20144 90037
YB.AT16
r=113km
E (Jm⁻³Hz⁻¹)
time (s)
b)
filter: (4.00Hz, 8.00Hz)
20140409003705
YB.AT05
r=35km
20140409003705
YB.AT11
r=39km
20140409003705
YB.AT04
r=62km
20140409003705
YB.AT09
r=81km
20140409003705
YB.AT18
r=84km
20140409003705
YB.AT17
r=89km
20140409003705
YB.AT16
r=113km
E (Jm⁻³Hz⁻¹)
time (s)

Figure 4.

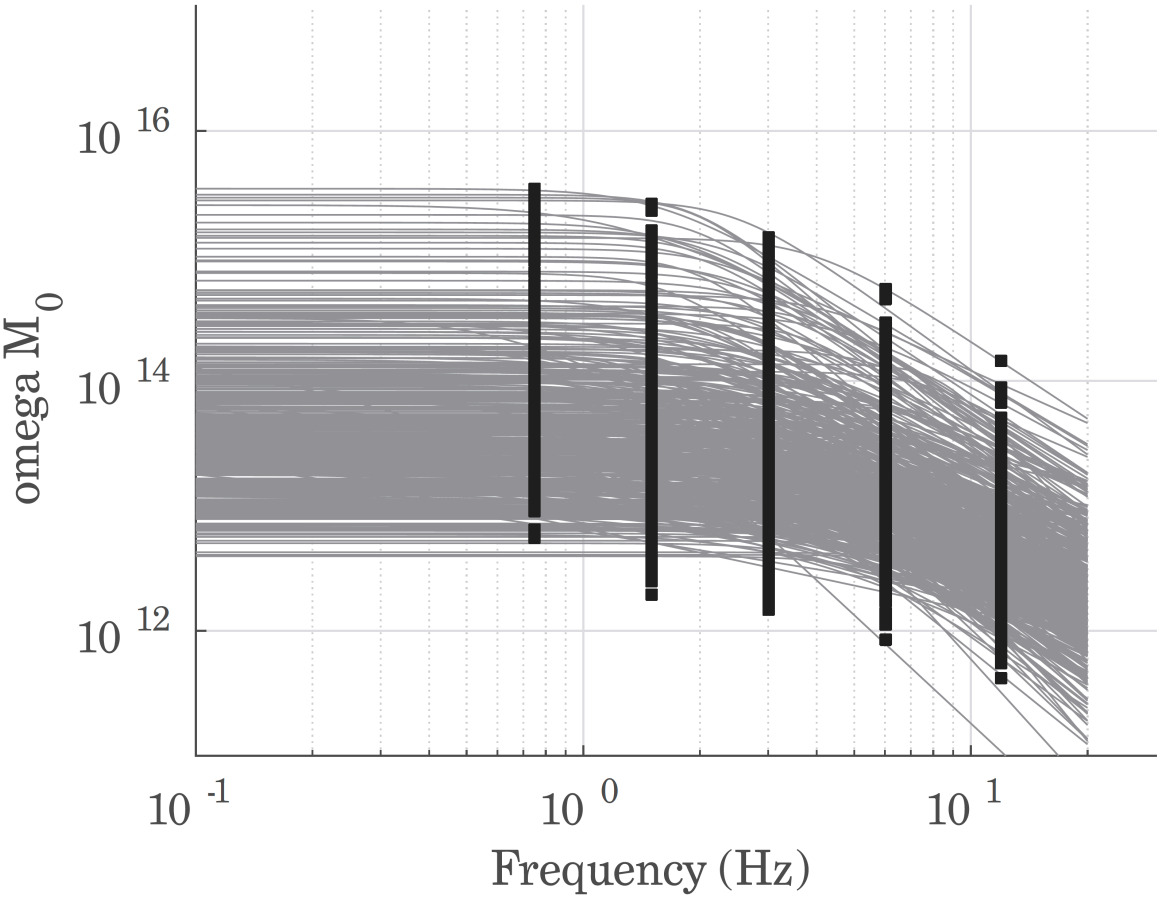

Figure 5.

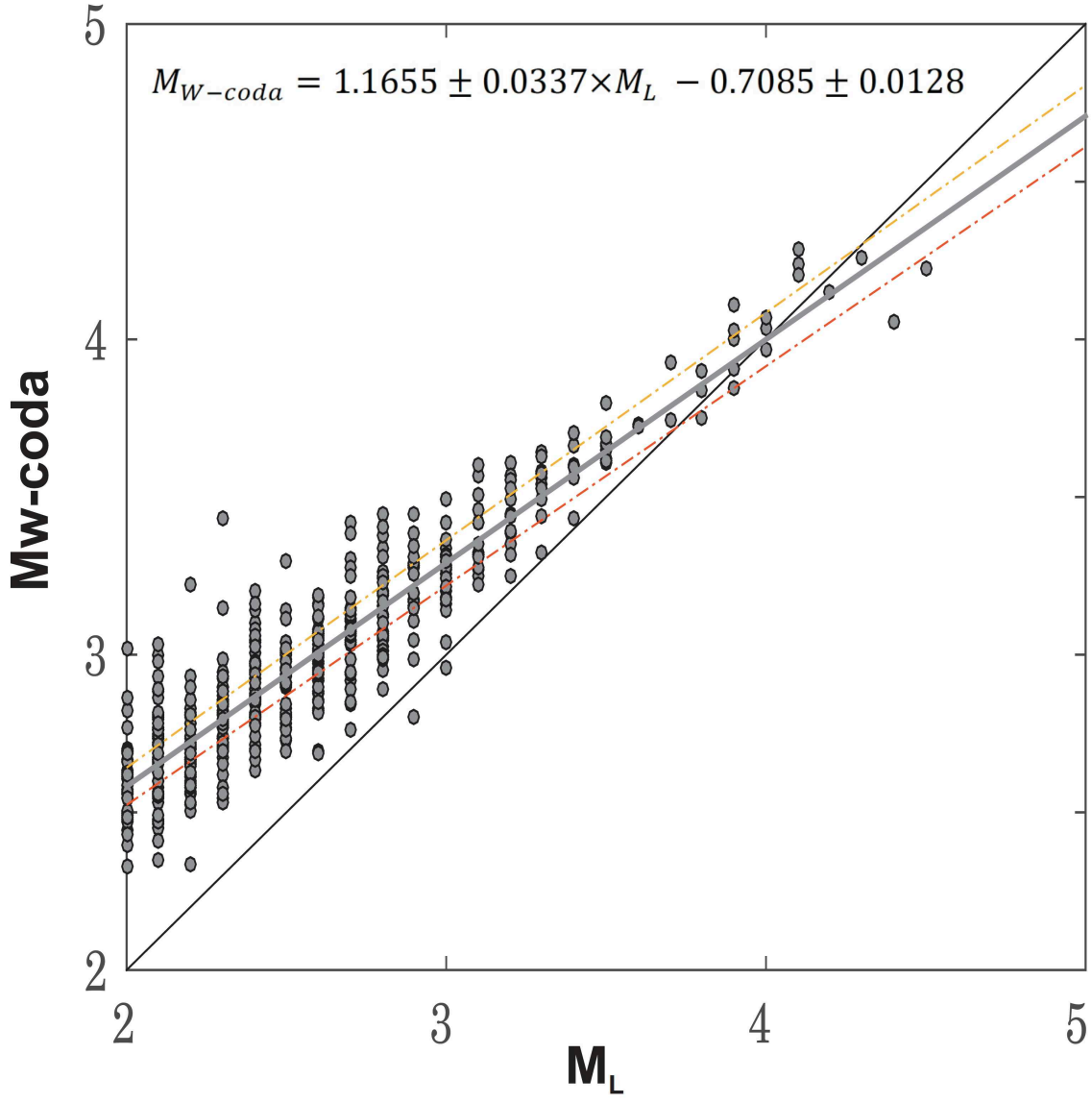

Figure 6.

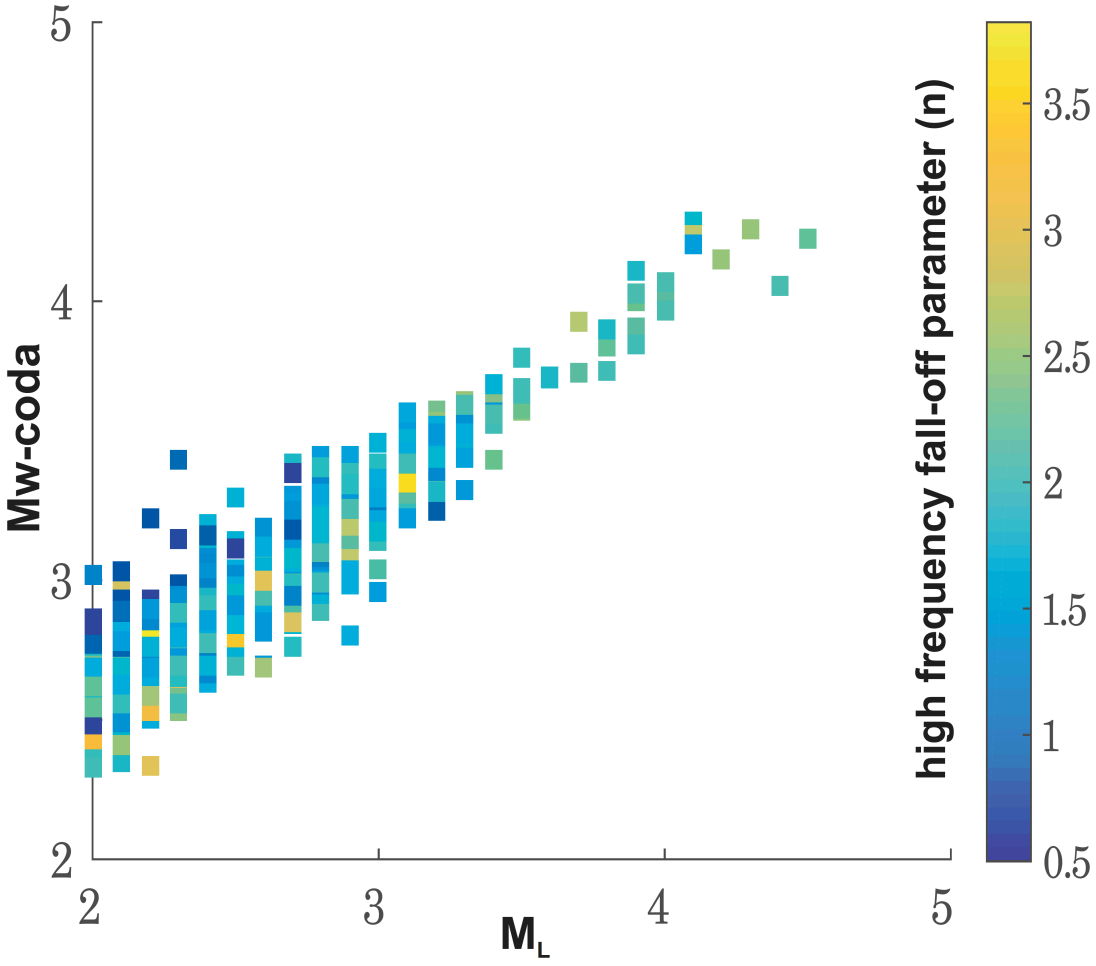
Mw-coda
M_L
high frequency fall-off parameter (n)
5
4
3
2
2
3
4
5
3.5
3
2.5
2
1.5
1
0.5

Figure 7.

Moment magnitude estimates for Central Anatolian earthquakes using coda waves

Tuna Eken[1]

[1]*Department of Geophysical Engineering, the Faculty of Mines, Istanbul Technical University, 34469 Maslak, Sarıyer, Istanbul, Turkey*

Abstract

Proper estimate of moment magnitude that is a physical measure of the energy released at earthquake source is essential for better seismic hazard assessments in tectonically active regions. Here a coda wave modeling approach that enables the source displacement spectrum modeling of examined event was used to estimate moment magnitude of central Anatolia earthquakes. To achieve this aim, three component waveforms of local earthquakes with magnitudes $2.0 \leq M_L \leq 5.2$ recorded at 72 seismic stations which have been operated between 2013 and 2015 within the framework of the CD-CAT passive seismic experiment. An inversion on the coda wave traces of each selected single event in our database was performed in five different frequency bands between 0.75 and 12 Hz. Our resultant moment magnitudes (M_W-coda) exhibit a good agreement with routinely reported local magnitude (M_L) estimates for study area. Apparent move-out that is, particularly, significant around the scattered variation of ML-MW-coda data points for small earthquakes (ML<3.5) can be explained by possible biases of wrong assumptions to account for anelastic attenuation and of seismic recordings with finite sampling interval. Finally, we present an empirical relation between M_W-coda and M_L for central Anatolian earthquakes.

Keyword(s): Coda waves modelling, seismic moment, moment magnitude, Radiative Transfer Theory

1. *Introduction*

The robust and stable knowledge of source properties (e.g. moment magnitude estimates) is crucial in seismically active countries such as Turkey for a better evaluation of seismic hazard potential as this highly depends on establishment of reliable seismicity catalogs. Moreover, accurate information on source parameters could be important when developing regional attenuation properties.

Conventional type of magnitude scales (M_L, m_b, M_S) as the result of empirically derived using direct wave analyses can be biased due to various effects such as source radiation pattern, directivity, and heterogeneities along the path since they may cause drastic changes in direct wave amplitude measurements (e.g., Favreau and Archuleta, 2003). Instead several early studies depending on the analysis of local and/or regional coda envelopes have indicated that coda wave amplitudes are significantly less variable by a factor of 3-to-5 compared to direct wave amplitudes (e.g., Mayeda and Walter, 1996; Mayeda et al., 2003; Eken et al., 2004; Malagnini et al., 2004; Gök et al., 2016). In fact local or regional coda waves that are usually considered to be generally to be composed of scattered waves and can be simply explained by that sample the single scattering model of Aki (1969) have been proven to be virtually insensitive to any source radiation pattern effect in contrast to direct waves because of the volume averaging property of the coda waves sampling the entire focal sphere (e.g., Aki and Chouet, 1975; Rautian and Khalturin, 1978). In Sato and Fehler (1998) and Sato et al. (2012) an extensive review study on the theoretical background of coda generation and advances of empirical observations and modelling efforts can be found in details.

There have been several approaches used for extracting information on earthquake source size via coda wave analyses. These approaches can be mainly divided into two groups. The first group of studies employs coda normalization strategy in which measurements require a correction for seismic attenuation parameters (e.g. intrinsic and scattering) that can be described by some empirical quality factors. To calibrate final source properties reference events are used to adjust measurements with respect to each other. For forward generation of synthetic coda envelopes, either single-backscattering or more advanced multiple-backscattering approximation are used. An example to this group is an empirical method originally developed by Mayeda et al. (2003) to investigate seismic source parameters such as energy, moment, and apparent stress drop in the western United States and in Middle East. They corrected observed coda envelopes for various influences, for instance, path effect, S-to-coda transfer function, site effect, and any distance-dependent changes in coda envelope shape. Empirical coda envelope method have been successfully applied to different regions with complicated tectonics such as northern Italy (e.g. Morasca et al., 2008), Turkey and Middle East (e.g. Eken et al., 2004; Gök et al. 2016); or Korean Peninsula (e.g. Yoo et al., 2013).

Second type of approach is a joint inversion technique that is based on a simultaneous optimization of source, path, and site specific terms via synthetic and observed coda envelope fitting within a selected time window including observed coda and direct-S wave parts. In this approach, the Radiative Transfer Theory (RTT) is employed for analytic expression of synthetic coda wave envelopes. The method that does not rely on coda normalization strategy was originally developed by Sens-Schönfelder and Wegler (2006) and successfully tested on local and regional earthquakes ($4 \leq Ml \leq 6$) detected by the German Regional Seismic Network. Further it has been applied to investigate source and frequency dependent

attenuation properties of different geological settings, i.e., Upper Rhine Graben and Molasse Basin regions in Germany and western Bohemia/Vogtland in Czechia (Eulenfeld and Wegler, 2016); entire United States (2017); central and western North Anatolian Fault Zone (Gaebler et al., 2018; Izgi et al., 2018). A more realistic earth model in which anisotropic scattering conditions were earlier considered by Gusev and Abubakirov (1987) yielded peak broadening effects of the direct seismic wave arrivals. This approach later was used in previous studies (e.g. Zeng, 1993; Przybilla and Korn, 2008; Gaebler et al., 2015) that dealt with propagation of P-wave elastic energy and the effect of conversion between P- and S-wave energies.

In the current work I present estimated source spectra as an output of a joint inversion of S- and coda waves parts of local earthquake waveforms 487 local earthquakes with magnitudes $2.0 < ML < 4.5$ detected in central Anatolia for their source parameters. The approach used here employs isotropic acoustic RTT approach for forward calculation of synthetic coda envelopes. Gaebler et al. (2015) has observed that modeling results from isotropic scattering were almost comparable with those inferred from relatively more complex elastic RTT simulations with anisotropic scattering conditions. The use of a joint inversion technique is advantageous since it is insensitive to any potential bias, which could be introduced by external information, i.e., source properties of a reference that is obtained separately from other methods for calibration. This is mainly because of the fact that we utilize an analytical expression of physical model involving source, and path related parameters to describe the scattering process. Moreover the type of optimization during joint inversion enables the estimates for source parameters of relatively small sized events compared to the one used in coda-normalization methods.

2. *Regional Setting and Data*

Present tectonic setting of Anatolia and surrounding regions have been mainly outcome of the northward converging movements among Africa, Arab, and Eurasian plates. To the west subducting African plate with a slab roll-back dynamics beneath Anatolia along Hellenic Trench has led to back-arc extension in the Aegean and western Anatolia while compressional deformation to the east around the Bitlis–Zagros suture was explained by collisional tectonics (e.g. Taymaz et al., 1990; Bozkurt, 2001) (Fig. 1). Central Anatolia is located between extensional regime to the west due to the subduction and compressional regime tectonics to the east due to the collisional tectonics. There are several fault systems responsible for ongoing seismic activity in the region. The major fault zone, the Central Anatolian Fault Zone (CAFZ) (Fig. 2), which primarily represents a transtensional fault structure with small amount of left-lateral offset during the Miocene (e.g. Koçyiğit and Beyhan, 1998), can be considered as a boundary between the carbonate nappes of the Anatolide-Tauride block from the highly deformed and metamorphosed rocks in the Kırşehir block. To the northwest of the CAFZ, Tuz Gölü Fault Zone (TGFZ) (Fig. 2), which is characterized by a right-lateral strike slip motion with a significant oblique-slip normal component, appears to be collocated with Tuz Gölü Basin sedimentary deposits as well as crystalline rocks within Kırşehir Block (e.g. Çemen et al., 1999; Bozkurt et al., 2001; Taymaz et al., 2004; Çubuk et al., 2014). At the southwest tip of the study region, the EAFZ generates large seismic activity that can be identified rather complicated seismotectonic setting: predominantly left-lateral strike-slip motion correlated well with the regional deformation pattern but also existing local clusters of thrust and normal faulting events on NS- and EW-trending subsidiary faults, respectively (Bulut et al., 2012). Such complicated behavior explains kinematic models of the shear deformation zone

126 evolution. It connects to the NAFZ at the Karlıova Triple Junction (Bozkurt, 2001) and to the
127 south splits into various segments nearby the Adana Basin (Kaymakci et al., 2006) (Fig. 2).
128 Toward the south, the EAFZ reaches the Dead Sea Fault Zone (DSFZ) that has a key role in
129 accommodating northward relative motions of Arabian and African Plates with respect to
130 Eurasia.
131
132 The present work utilizes three-component waveforms of local seismic activity detected at 72
133 broadband seismic stations (Fig. 2) that have been operated for 2 years between 2013 and
134 2015 within the framework of a temporary passive seismic experiment, the Continental
135 Dynamics–Central Anatolian Tectonics (CD-CAT) (Portner et al., 2018). We benefit from
136 revisited standard earthquake catalogue information (publicly available at
137 http://www.koeri.boun.edu.tr) to extract waveform data for a total of 2231 examined events
138 with station-event pair distance less than 120 km and focal depths less than 10 km. Most of
139 the detected seismic activity in the study area is associated to several fault zones in the region,
140 i.e., the EAFZ, CAFZ, DSFZ, TGFZ, etc. Here we note that selection of only local
141 earthquakes is to exclude possible biases, which may be introduced by Moho boundary
142 guided Sn-waves while upper crustal earthquakes are preferred in this study to exclude effect
143 of relatively large-scale heterogeneities on coda wave trains. Finally a visual inspection
144 conducted over all waveforms to ensure high-quality waveforms reduces our event number to
145 1193. Selected station and event distributions can be seen in Figure 2.
146
147 Observed waveforms were prepared at 5 different frequency bands with central frequencies at
148 0.75, 1.5, 3.0, 6.0, 12.0 Hz via a Butterworth band-pass filtering process. In the next step, we
149 applied Hilbert transform to filtered waveform data in order to obtain the total energy
150 envelopes. An average crustal velocity model was used to predict P and S wave onsets on

envelopes and then based on this information: (i) the noise level prior to the P-wave onset was eliminated (ii) S-wave window was determined starting at 3s prior to and 7 s afterwards S-wave onset as this allowed to include all direct S-wave energy, (iii) starting at the end of the S-wave window, a coda window of 100s at maximum was determined. Length of coda windows can be shorter when signal-to-noise ratio (SNR) is less than 2.5 or when the same window consists of coda waves from two earthquakes, which can give rise to a decline in the envelope. We omit the earthquakes with less than 10 s of coda length from our database.

3. Method

We adopted an inversion procedure that was originally developed by Sens-Schönfelder and Wegler (2006) and later modified by Eulenfeld and Wegler (2016). The forward part, which involves calculation of energy density for a specific frequency band caused by an isotropic source, is expressed in Sens-Schönfelder and Wegler (2006) as follows:

$$E_{mod}(t,r) = WR(r)G(t,r,g)e^{-bt} \qquad (1)$$

where W gives source term and it is frequency dependent. R(r) indicates the energy site amplification factor and b is intrinsic attenuation parameter. $G(t,r,g)$ represents Green's function that includes scattered wave field as well as direct wave and its expression is given by Paasschens (1997) as follows:

$$G(t,r,g) = e^{(-v_0 t g_0)}\left[\frac{\delta(r-v_0 t)}{4\pi r^2} + \left(\frac{4\pi v_0}{3g_0}\right)^{-\frac{3}{2}} t^{-\frac{3}{2}} \times \left(1-\frac{r^2}{{v_0}^2 t^2}\right)^{\frac{1}{8}} K\left(v_0 t g_0\left(1-\frac{r^2}{{v_0}^2 t^2}\right)^{\frac{3}{4}}\right) H(v_0 t - r)\right] \qquad (2)$$

Here the term within Dirac delta function represents direct wave and other term indicates

scattered waves. v_0 describes the mean S-wave velocity while g_0 is the scattering coefficient.

Possible discrepancy between predicted (Eq. 1) and observed energy densities for each event at each station with N_{ij} time samples (index k) in a specific frequency band can be minimized using:

$$\epsilon(g) = \sum_{i,j,k}^{N_S,N_S,N_{ij}} \left(lnE_{ijk}^{obs} - lnE_{ijk}^{mod}(g)\right)^2 \quad (3)$$

Here, the number of stations (index i) and events (index j) are shown by N_S and N_E, respectively. Optimization of g will be achieved when

$$lnE_{ijk}^{obs} = lnE_{ijk}^{mod} \qquad (4) \qquad \text{or}$$

$$lnE_{ijk}^{obs} = \ln Gt_{ijk}, r_{ijk}, g + lnR_i + lnW_j - bt_{ijk} \qquad (5)$$

Equation 5 simply define an overdetermined inversion problem with $\sum_{i,j} N_{ij}$ number equation systems and with $N_S + N_E + 1$ variables and thus b, R_i, and W_j can be solved via a least-squares technique. $\epsilon(g)$ can be defined as sum over the squared residuals of the solution.

Eulenfeld and Wegler (2016) present a simple recipe to perform inversion:

(i) Calculate Green's functions through the analytic approximation of the solution for 3-D isotropic radiative transfer (e.g. Paasschens 1997; Sens-Schönfelder and Wegler, 2006) by using fixed scattering parameters and minimize equation 5 to solve for b, R_i, and W_j via a weighted least-squares approach.

(ii) Calculate $\epsilon(g)$ using equation 3.

195 (iii) Repeat (i) and (ii) by selecting different g to find the optimal parameters g, b, R_i and W_j
196 that finally minimize the error function ϵ.

197 In Fig. 3 an example for the minimization process that was applied at five different frequency
198 bands is displayed for one selected event at recorded stations of the CD-CAT project.

199 Minimization described above for different frequencies will yield unknown spectral source
200 energy term, W_j as well as site response, R_i and attenuation parameters, b, and g that will
201 satisfy optimal fitting between observed and predicted coda wave envelopes. Example for this
202 fitting can be seen in Figure 4. The present study deals with frequency dependency of W_j
203 since this information can be later useful to obtain source displacement spectrum and thus
204 seismic moment and moment magnitudes of analyzed earthquakes using the formula of the *S*-
205 wave source displacement spectrum for a double-couple source in the far-field, which is given
206 by Sato et al. (2012):

207 $$\omega M(f) = \sqrt{\frac{5\rho_0 v_0^5 W}{2\pi f^2}} \quad (6)$$

208

209 The relation between the obtained source displacement spectrum and seismic moment value
210 was earlier described in Abercrombie (1995) by:

211 $$\omega M(f) = M_0 \left(1 + \left(\frac{f}{f_c}\right)^{\gamma n}\right)^{-\frac{1}{\gamma}} \quad (7)$$

212 where n is related to the high-frequency fall-off and γ is known as shape parameter that
213 controls the sharpness of spectrum at corner frequency between the constant level M_0 (low
214 frequency part) and the fall-off with f^{-n} (high frequency part). Taking logarithm of equation 7
215 gives:

$$\ln \omega M(f) = lnM_0 - \frac{1}{\gamma}\ln\left(1 + \left(\frac{f}{f_c}\right)^{\gamma c}\right) \quad (8)$$

Eq. 8 describes an optimization problem of which data forms observed source displacement spectrum and four source parameters, M_0, γ, n, and f_c are the unknown model parameters that can be resolved in a simultaneous least-squares inversion of the equation 8. Finally moment magnitude, M_W can be calculated from modeled source parameters, seismic moment, M_0 using a formula given by Hanks and Kanamori (1979):

$$M_w = \frac{2}{3} log_{10} M_0 - 6.07 \quad (9)$$

4. Results and Discussions

4.1 Coda wave source spectra

Figure 5 displays observed values of source spectra established by inserting inverted spectral source energy term W at each frequency in Eq. 6 for all analyzed events. Each curve in this figure represents model spectrum estimate based on inversion procedure described in previous section. Modeled spectrum characteristics computed for 487 local earthquakes of which lateral distribution is presented in Figure 2 suggest, in general, that we were able to obtain typically expected source displacement spectrum with a flat region around the low frequency limit and decaying behaviour above a corner frequency.

Owing to the multiple-scattering process within small scale heterogeneities that makes coda waves gain an averaging nature, the variation in coda amplitudes due to differences source radiation pattern and path effect are reduced (Walter et al., 1995; Mayeda et al., 2003). Eulenfeld and Wegler (2016) found that radiation pattern would have only a minor influence

241 on the S-wave coda while it might disturb attenuation models inferred from the direct S-wave
242 analyses unless the station distribution relative to the earthquakes indicates a good azimuthal
243 coverage. A peak-like source function assumption for small earthquakes that are utilized in
244 the present work was earlier proven to be adequate in early application of the coda-wave
245 fitting studies (e.g. Sens-Schönfelder and Wegler, 2006; Gaebler et al., 2015; and Eulenfeld
246 and Wegler, 2016).
247
248 Conventional approaches (e.g. Abercrombie, 1995; Kwiatek et al., 2011) to estimate source
249 parameters such as corner frequency, seismic moment, high-frequency fall-off through fitting
250 of observed displacement spectra observed at a given station in an inversion scheme could be
251 misleading since these methods usually: (i) assume a constant value of attenuation effect (no
252 frequency variation) defined by a factor exp ($-\pi ftQ^{-1}$) over the spectrum, (ii) and assume
253 omega-square model with a constant high-frequency fall-off parameter, n=2. Following Sens-
254 Schönfelder and Wegler (2006) and Eulenfeld and Wegler (2016), however, we estimate
255 attenuation parameters (intrinsic and scattering) seperately within a simultaneous inversion
256 procedure in which high-frequency fall-off parameter varies. This is fairly consistent with
257 early studies (e.g. Ambeh and Fairhead, 1991; Eulenfeld and Wegler, 2016) where significant
258 deviations from the omega square model (n>3) were reported implying that the omega-square
259 model as a source model for small earthquakes must be reconsidered in its general
260 acceptance. Earlier it has been well-observed that the source spectra, especially, for large
261 earthquakes could be better explained by models of two corner frequencies (e.g.,
262 Papageorgiou and Aki, 1983; Joyner, 1984; Atkinson, 1990). Recently, Denolle et al. (2016)
263 observed that conventional spectral model of a single-corner frequency and high-frequency
264 fall-off rate could not explain P wave source spectra of thrust earthquakes with magnitude
265 Mw 5.5 and above. Instead, they suggested the double-corner-frequency model for large

266 global thrust earthquakes with a lower corner frequency related to source duration and with an
267 upper corner frequency suggesting a shorter time scale unrelated to source duration, which
268 exhibits its own scaling relation. Uchide and Imanishi (2016) reported similar differences
269 from the omega-square model would be valid also for smaller earthquakes by using spectral
270 ratio technique that involves empirical Green's function (EGF) events to avoid having a
271 complete knowledge of path and site effects for shallow target earthquakes (M_W 3.2–4.0) in
272 Japan. The source spectra for many of the target events in their study suggested a remarkable
273 discrepancy from the omega-square model for relatively small earthquakes. They explained
274 such differences by incoherent rupture due to heterogeneities in fault properties and applied
275 stress, the double-corner-frequency model, and possibility of a high-frequency falloff
276 exponent value slightly higher than 2. In our case, the smallest event was with M_W-coda
277 larger than 2.0, thus we had no chance to make a similar comparison, however, high-
278 frequency fall-off parameters varied from n=0.5 to n=4. A notable observation in the
279 distribution of n was n=2 or n=2.5 would be better explained for earthquakes with M_W-coda
280 >4.0 whereas the smaller magnitudes exhibited more scattered pattern of variation in n
281 (Figure 7). Eulenfeld and Wegler (2016) claimed that the use of separate estimates of the
282 attenuation or correction for path effect via emprically determined Green's function would be
283 better strategy in order to invert station displacement spectra for source parameters. This is
284 mainly because smaller earthquakes (with n>2), in particular, assuming omega-square model
285 can distort the estimates of corner frequency and even seismic moment especially in regions
286 where Q is strongly frequency dependent.
287
288 *4.2 Coda wave –derived magnitude vs. M_L catalogue magnitude*
289 A scatter plot between catalogue magnitudes based on local magnitudes (M_L) and our coda-
290 derived magnitudes (M_W-coda) that are inferred from resultant frequency dependent source

displacement spectra and thus seismic moment (e.g. Eq. 9) is shown in Fig. 6. Such comparison suggests an overall coherency between both types of magnitudes. This implies very simple model of a first-order approximation for S-wave scattering with isotropic acoustic radiative transfer approach can be efficient to link the amplitude and decaying character of coda wave envelopes to the seismic moment of the source.

In the present study, a linear regression analyses performed between M_W-coda and M_L magnitudes (Fig. 5) resulted in an emprical formula that can be employed to convert local magnitudes into coda-derived moment magnitude calculation of local earthquakes in this region:

$$M_{W-coda} = 1.1655 \pm 0.0337 \times M_L - 0.7085 \pm 0.0128 \quad (10)$$

Bakun and Lindh (1977) empirically described the linear log seismic moment-local magnitude relation between seismic moments (Mo) and local magnitudes (M_L) for earthquakes near Oroville, California. Beside this several other studies investigated to find an optimum relation between M_W and M_L by implementing linear and/or non-linear curve-fitting approaches. Malagnini and Munafò (2018) proposed two different linear fits separated by a crossover M_L=4.31 could represent M_L-M_W data points obtained from earthquakes of the central and northern Apennines, Italy. Several coefficient of regression analyses in their fits account for the combined effects of source scaling and crustal attenuation as well as regional attenuation, focal depth, and rigidity at source. Goertz-Allmann et al. (2011), for instance, introduced hybrid type of scaling relation that is linear below M_L 2 and above M_L 4 and a quadratic relation in between ($2 \leq M_L \leq 4$) for earthquakes in Switzerland detected between 1998 and 2009. Edwards and Rietbrock (2009) employed a second-order polynomial equation

316 to relate local magnitudes routinely reported in the Japan Meteorological Agency (JMA)
317 magnitude and moment magnitude. More recently, using multiple spectral ratio analyses
318 Uchide and Imanishi (2018) estimated relative moment magnitudes for the Fukushima
319 Hamadori and the northern Ibaraki prefecture areas of Japan and reported a quadratic form of
320 correlation between JMA magnitudes and moment magnitudes. Resultant empirical curve in
321 Uchide and Imanishi (2018) implied a considerable discrepancy between the moment
322 magnitudes and the JMA magnitudes, with a slope of 1/2 for microearthquakes suggesting
323 possible biases introduced by anelastic attenuation and the recording by a finite sampling
324 interval.
325
326 Apparent move-out in Fig. 5 and Eq. 10, presumably stems from the use of different
327 magnitude scales for comparison. Conventional magnitudes scales such as M_L, mb inferred
328 from phase amplitude measurements are seemingly sensitive to attenuation and 2D variation
329 along the path (Pasyanos et al., 2016). Unlike local magnitude scales, seismic moment-based
330 moment magnitude (M_W) essentially represents a direct measure of the strength of an
331 earthquake caused by fault slip and is estimated from relatively flat portion of source spectra
332 at lower frequencies that can be less sensitive to the near surface attenuation effects. The
333 consistency between coda-derived moment magnitude and local magnitude scales for the
334 earthquakes with M_W-coda > 3.0 indicates that our non-empirical approach successfully
335 worked in this tectonically complex region. This observation is anticipated, for relatively
336 large earthquakes, since more energy will be characteristic at lower frequencies. We
337 observed similar type of consistency in early studies that investigate source properties of local
338 and regional earthquakes based on emprical coda methods with simple 1-D radially
339 symmetric path correction (e.g. Eken et al., 2004; Gök et al., 2016). Coda waves–derived
340 source parameters were obtained with high-precision in Mayeda et al. (2005), Phillips et al.

(2014), Pasyanos et al. (2016) following the use of 2-D path-corrected station techniques to consider the amplitude-distance relationships. Observable outliers in Figure 5, for the events with less than Mw 3.5, however, can be attributed to the either possible biases on local magnitude values taken from the catalogue or small biases on our intrinsic (Q_i^{-1}) and scattering (Q_s^{-1}) attenuation terms. One another possible contribution to such mismatch might be associated to the influences of mode conversions between body and surface waves or surface-to-surface wave scattering (e.g. Wu & Aki 1985) that are not restricted to low frequencies (<1Hz) (Sens-Schönfelder and Wegler, 2006).

5. Conclusions

This study provides an independent solution for estimating seismic source parameters such as seismic moment and moment magnitude for local earthquakes in central Anatolia without requiring *a priori* information on reference events with waveform modelling results to be used for calibration or *a priori* information on attenuation for path effect corrections. In this regard, the approach used here can be easy and useful tool for investigation of source properties of local events detected at temporal seismic networks. Moreover, seismic moment can be approximated via waveform modelling methods but due to the small-scale heterogeneities of the media that waves propagate, it is often a hard task to establish Green's function for small earthquakes (M_L < 3.5). An analytical expression of energy density Green's function in a statistical manner employed in the present work enables neglecting the interaction of the small-scale inhomogeneities with seismic waves as this can be practical for seismic moment calculations of small events that may pose source energy at high-frequency. It is noteworthy to mention that our isotropic scattering assumption does not consider anisotropic case, which could be valid for real media, but still provides a simple and effective tool to define the transport for the anisotropic case since the estimated scattering coefficient

can be interpreted as transport scattering coefficient. An averaging over S-wave window enables to overcome biases caused by using unrealistic Green's function (Gaebler *et al.* 2015). Since the present study mainly focuses on source properties of local earthquakes in the study area, scattering and intrinsic attenuation properties that are other products of our coda envelope fitting procedure will be examined in details within a future work. Finally, the empirical relation developed between M_W-coda and M_L will be a useful tool for quickly converting catalogue magnitudes to moment magnitudes for local earthqukes in the study area.

Data and resources

The python code used for carrying out the inverse modeling is available under the permissive MIT license and is distributed at https://github.com/trichter/qopen. We are grateful to the IRIS Data Management Center for maintaining, archiving and making the continuous broadband data used in this study open to the international scientific community.

Acknowledgement

The facilities of IRIS Data Services, and specifically the IRIS Data Management Center, were used for access to waveforms, related metadata, and/or derived products used in this study. IRIS Data Services are funded through the Seismological Facilities for the Advancement of Geoscience and EarthScope (SAGE) Proposal of the National Science Foundation under Cooperative Agreement EAR-1261681. Data for the CD-CAT experiment (https://doi.org/10.7914/SN/YB_2013) are available from the IRIS Data Management Center at http://www.iris.edu/hq/. Tuna Eken acknowledge financial support from Alexander von Humboldt Foundation (AvH) towards computational and peripherals resources. I am grateful to the Topical Editor Charlotte Krawczyk for handling the revision process and Takahiko

391 Uchide for his valuable opinions on the improvement of manuscript.

392 *References*

393 Abercrombie, R.E.: Earthquake source scaling relationships from −1 to 5 ML using
394 seismograms recorded at 2.5-km depth, J. geophys. Res., 100(B12), 24 015–24 036,
395 1995.
396 Aki, K., and Chouet., B.: Origin of coda waves: Source, attenuation, and scattering effects, J.
397 Geophys. Res. 80, 3322–3342, 1975.
398 Atkinson, G. M.: A comparison of eastern North American ground motion observations with
399 theoretical predictions, Seismol. Res. Lett. 61, 171–180, 1990.
400 Bakun, W.H. and Lindh, A.G.: Local Magnitudes, Seismic Moments, and Coda Durations for
401 Earthquakes Near Oroville, California, Bulletin of the
402 SeismologicalSocietyofAmerica.Vol.67,No.3, pp. 615-629, 1977.
403 Bozkurt, E.: Neotectonics of Turkey—A synthesis: Geodinamica Acta, v. 14, p. 3–30, 2001.
404 Bulut, F., Bohnhoff, M., Eken, T., Janssen, C., Kılıç, T., and Dresen, G.: The East Anatolian
405 fault zone: Seismotectonic setting and spatiotemporal characteristics of seismicity based
406 on precise earthquake locations: Journal of Geophysical Research, v. 117, B07304,
407 https://doi .org/10.1029/2011JB008966, 2012.
408 Çemen, I., Göncüoglu, M.C., and Dirik, K.: Structural evolution of the Tuz Gölü basin in central
409 Anatolia, Turkey: Journal of Geology, v. 107, p. 693–706, https://doi.org/10.1086
410 /314379, 1999.
411 Çubuk Y, Yolsal-Çevikbilen S, Taymaz, T.: Source parameters of the 20052008 Balˆa Sirapinar
412 (central Turkey) earthquakes: Implications for the internal deformation of the Anatolian
413 plate. Tectonophysics 635(Supplement C) :125 – 153, 2014.
414 Denolle, M. A., and Shearer, P.M.: New perspectives on self-similarity for shallow thrust
415 earthquakes, *J. Geophys. Res. Solid Earth*, *121*, 6533–6565, 2016.

416 Edwards, B., & Rietbrock, A.: A comparative study on attenuation and source-scaling relations
417 in the Kantō, Tokai, and Chubu regions of Japan, using data from Hi-net and KiK-net.
418 Bulletin of the Seismological Society of America, 99, 2435–2460, 2009.

419 Eken, T., Mayeda, K., Hofstetter, A., Gök, R., Orgülü, G. and Turkelli, N.: An application of the
420 coda methodology for moment-rate spectra using broadband stations in Turkey.
421 Geophys. Res. Lett, 31, L11609, 2004.

422 Eulenfeld, T. and Wegler, U.: Measurement of intrinsic and scattering attenuation of shear
423 waves in two sedimentary basins and comparison to crystalline sites in Germany,
424 Geophys J Int., 205(2):744-757, 2016.

425 Eulenfeld, T. and Wegler, U.: Crustal intrinsic and scattering attenuation of high-frequency
426 shear waves in the contiguous United States. J Geophys., Res, 122, 2017.

427 Favreau, P., and Archuleta, R.J.: Direct seismic energy modelling and application to the 1979
428 Imperial Valley earthquake, Geophys. Res. Lett., 30, 1198, 2003.

429 Gaebler, P.J., Eulenfeld, T. & Wegler, U.: Seismic scattering and absorption parameters in the
430 W-Bohemia/Vogtland region from elastic and acoustic radiative transfer theory,
431 Geophys. J. Int., 203(3), 1471–1481, 2015.

432 Gaebler, P.J., Eken, T., Bektaş, H.Ö, Eulenfeld, T., Wegler, U., Taymaz, T.: Imaging of Shear
433 Wave Attenuation Along the Central Part of the North Anatolian Fault Zone, Turkey,
434 submitted to the Journal of Seismology, 2018.

435 Goertz-Allmann, B. P., Edwards, B., Bethmann, F., Deichmann, N., Clinton, J., Fäh, D., &
436 Giardini, D.: A new empirical magnitude scaling relation for Switzerland. Bulletin of the
437 Seismological Society of America, 101, 3088–3095, 2011.

438 Gök, R., Kaviani, A., Matzel, E. M., Pasyanos, M. E., Mayeda, K., Yetirmishli, G., El-Hussain,
439 I., Al-Amri, A., Al-Jeri, F., Godoladze, T., Kalafat, D., Sandvol, E. A., and Walter,

440 W.R.: Moment Magnitudes of Local/Regional Events from 1D Coda Calibrations in the
441 Broader Middle East Region. Bull Seismol Soc Am., 106(5):1926-1938, 2016.
442 Gusev, A.A. & Abubakirov, I.R.: Simulated envelopes of non-isotropically scattered body
443 waves as compared to observed ones: another manifestation of fractal heterogeneity,
444 Geophys. J. Int., 127(1), 49–60, 1996.
445 Hanks, T.C. and Kanamori, H.: A moment magnitude scale, J. Geophys., Res., 84, 2348–2350,
446 1979.
447 Izgi, G., Eken, T., Gaebler, P., and Taymaz, T.: Frequency-Dependent Shear Wave Attenuation
448 Along the Western Part of the North Anatolian Fault Zone, Geophysical Research
449 Abstracts, Vol. 20, EGU2018-629-2, 2018.
450 Kaymakci, N. Inceöz, M. Ertepinar, P.: 3D architecture and Neogene evolution of the Malatya
451 Basin: inferences for the kinematics of the Malatya and Ovacik Fault Zones. Turkish
452 Journal of Earth Sciences, 15, 123-154, 2006.
453 Kwiatek, G., Plenkers, K. & Dresen, G.: 2011. Source parameters of pico-seismicity recorded at
454 Mponeng Deep Gold Mine, South Africa: implications for scaling relations, Bull. seism.
455 Soc. Am., 101(6), 2592–2608, 2011.
456 Malagnini, L., Mayeda, K., Akinci, A., and Bragato, P. L.: Estimating absolute site effects,
457 Bull. Seismol. Soc. Am. 94, no. 4, 1343–1352, 2004.
458 Malagnini, L., and Munafò., I.: On the Relationship between M_L and Mw in a Broad Range: An
459 Example from the Apennines, Italy, Bulletin of the Seismological Society of America,
460 Vol. 108, No. 2, pp. 1018–1024, 2018.
461 Mayeda, K., and Walter, W.R.: Moment, energy, stress drop, and source spectra of western
462 United States earthquakes from regional coda envelopes, J. Geophys. Res. 101, 11,195–
463 11,208, 1996.

464 Mayeda, K., Hofstetter, A., O'Boyle, J.L., and Walter, W.R.: Stable and transportable regional
465 magnitudes based on coda-derived moment-rate spectra, Bull. Seismol. Soc. Am. 93,
466 224–239: 2003.

467 Mayeda, K., Malagnini, L., Phillips, W. S., Walter, W. R., and Dreger, D.: 2D or not 2D, that is
468 the question: A Northern California Test. Geophys- ical Research Letters, 32(12), 2005.

469 Morasca, P., Mayeda, K., Malagnini, L. and Walter,W.R.: Coda and direct-wave attenuation
470 tomography in northern Italy, Bull Seismol Soc Am., v. 98, pages, 1936-1946, 2004.
471 Morasca, P., Mayeda, K., Gök, R., Phillips, W.S., and Malagnini, L.: Coda-derived source
472 spectra, moment magnitudes and energy-moment scaling in the western Alps, Geophys.
473 J. Int., 160, 263–275, 2008.
474 Paasschens, J.: Solution of the time-dependent Boltzmann equation, Phys. Rev. E, 56(1), 1135–
475 1141, 1997.
476 Papageorgiou, A., and Aki, K.: A specific barrier model for the quantitative description of
477 inhomogeneous faulting and the prediction of strong ground motion I: Description of the
478 model, Bull. Seismol. Soc. Am., 73(3), 693–722, 1983.
479 Pasyanos, M. E., R. Gök, and Walter, W.R.: 2-D variations in coda amplitudes in the Middle
480 East. Bull. Seismol. Soc. Am. 106, no. 5, 2016.
481 Phillips, W. S., Mayeda, K. M., and Malagnini, L.: How to invert multi-band, regional phase
482 amplitudes for 2-d attenuation and source parameters: Tests using the usarray. Pure and
483 Applied Geophysics, 171(3):469-484, 2014.
484 Portner, D.E., Delph, J.R., Biryol, C.B., Beck, S.L., Zandt, G., Özacar, A.A., Sandvol, E., and
485 Türkelli, N.: Subduction termination through progressive slab deformation across
486 Eastern Mediterranean subduction zones from updated P-wave tomography beneath
487 Anatolia, Geosphere, 14(3): 907-925, 2018.

Przybilla, J. and Korn, M.: Monte Carlo simulation of radiative energy transfer in continuous elastic random mediathree-component envelopes and numerical validation. Geophys J Int , 173(2):566-576, 2008.

Rautian, T.G. & Khalturin, V.I.: The use of the coda for determination of the earthquake source spectrum, Bull. Seism. Soc. Am., 68(4), 923–948, 1978.

Sato, H. and Fehler, M.C.: Seismic Wave Propagation and Scattering in the Heterogeneous Earth, Springer-Verlag, New York, 1998.

Sato, H., Fehler, M.C. & Maeda, T. Seismic Wave Propagation, and Scattering in the Heterogeneous Earth, 2nd edn, Springer: 2012.

Sens-Schönfelder, C. and Wegler, U.: Radiative transfer theory for estimation of the seismic moment. Geophys J Int, 167(3):1363-1372.

Taymaz, T., Jackson, J., Westaway, R.: Earthquake mechanisms in the Hellenic Trench near Crete. Geophys. J. Int.102, 695–731, 1990.

Taymaz, T., Westaway, R., Reilinger, R.: Active faulting and crustal deformation in the eastern Mediterranean Region. Spec. Issue Tectonophys. 391 (1-4), 1–9. http:// dx.doi.org/10.1016/j.tecto.2004.07.005, 2004.

Uchide, T., & Imanishi, K.: Small earthquakes deviate from the omega-square model as revealed by multiple spectral ratio analysis. Bulletin of the Seismological Society of America, 106(3), 1357–1363, 2016.

Uchide, T., & Imanishi, K.: Underestimation of microearthquake size by the magnitude scale of the Japan Meteorological Agency: Influence on earthquake statistics. Journal of Geophysical Research: Solid Earth, 123, 606–620, 2018.

Yoo, S.-H., Rhie, J., Choi, H.-S., and Mayeda, K.: Coda-derived source parameters of earthquakes and their scaling relationships in the Korean Peninsula, Bull. Seismol. Soc. Am., 101, 2388–2398, 2011.

513 Wu, R. and Aki, K.: The fractal nature of the inhomogeneities in the lithosphere evidenced from
514 seismic wave scattering, Pure appl. Geophys., 123(6), 805–818, 1985.
515 Zeng, Y., Su, F. and Aki, K.: Scattering wave energy propagation in a random isotropic
516 scattering medium: 1. Theory, J. Geophys. Res., 96(B1), 607–619, 1991.
517

518 *Figure Captions*

519 Figure 1. Major tectonic features of Turkey and its adjacent. The plate boundary data used
520 here is taken from Bird (2003). Subduction zones are black, continental transform faults are
521 red, continental rift boundaries are green, and spreading ridges boundaries are yellow. NAFZ,
522 EAFZ, and DSFZ are the North Anatolian Fault, East Anatolian Fault, and the Dead Sea fault,
523 respectively.
524

525 Figure 2. Epicentral distribution of all local events selected from the study area in the KOERI
526 catalogue. Gray circles represent earthquakes with poor quality that are not considered for the
527 current study while black indicates the location of local events with good quality. Red circles
528 among these events are 487 events used in coda wave inversion since they are successful at
529 passing quality criteria of further pre-processing procedure.
530

531 Figure 3. An example from the inversion procedure explained in chapter 3. Here coda
532 envelope fitting optimization is performed on band-pass filtered (8-16Hz) digital recordings
533 of an earthquake (2014 April 09, M_W-coda3.2) extracted for 7 seismic stations that operated
534 within the CD-CAT array. Large panel at the lower left-hand side displays the error function ε
535 as a function of g_0. Thick blue cross here represent the optimal value of $g = g_0$. Other small
536 panels at upper and right-hand side show the least- squares solution of the weighted linear
537 equation system for the first 6 guesses and optimal guess for g_0. There dots and gray curves

indicate the ratio between energy (E^{obs}) and the Green's function (G) obtained for direct S-waves and observed envelopes at various stations, respectively. Please notice that during this optimization process envelopes are corrected for the obtained site corrections R_i. The slope of linear curve at each small panel yields −b and while its intercept W are the intrinsic attenuation and source related terms at the right-hand side of equation 5 part of the right-hand side of the equation system.

Figure 4. a) Results of the inversion of the 2014-April-09, M_W-coda3.2 earthquake: Sample fits between observed and calculated energy densities in the frequency band 0.5–1.0 Hz are given for 6 different stations (see upper right corner for event ID, station name, and distance to hypocenter). Note that light blue curves represent observed envelope. Smoothed observed calculated envelopes in each panel are presented by blue and red curves, respectively. Blue and red dots exhibit location of the average value for observed and calculated envelopes within the S-wave window, respectively. b) The same as in (a) obtained in the frequency band 4.0–8.0 Hz.

Figure 5. All individual observed (black squares) and predicted (gray curve) source displacement spectra observed at 72 stations from 487 local earthquakes in central Anatolia.

Figure 6: Scatter plot between local magnitudes (M_L) of analyzed events with coda waves-derived magnitudes (M_W-coda) of the same events. The outcome of a linear regresssion analysis yielded an emprical formula (e.g. Eq. ~~9~~10) to identify the overall agreement represented by gray straight line. Yellow and red dashed lines indicate upper and lower limit of linearly fitting to that scatter.

Figure 7: Same scatter plot displayed in Fig. 6 color coded by estimated high-frequency fall-off parameter for each inverted event.

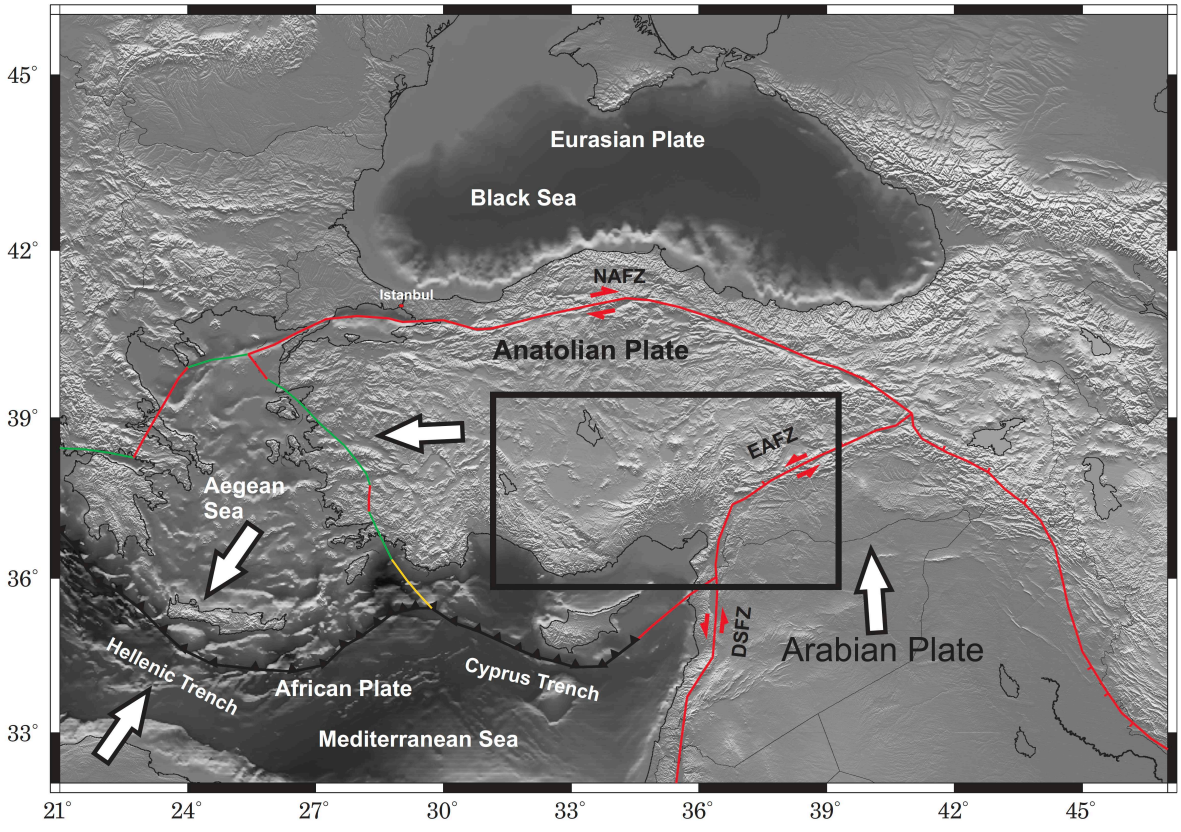

Figure 1.

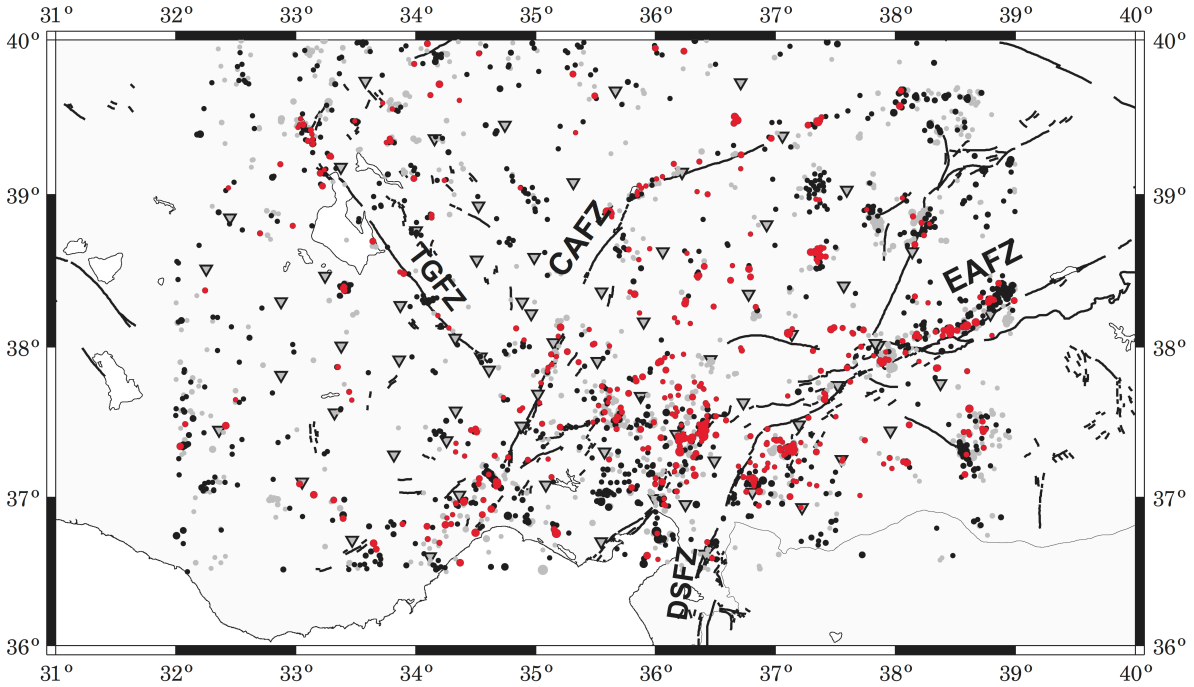

Figure 2.

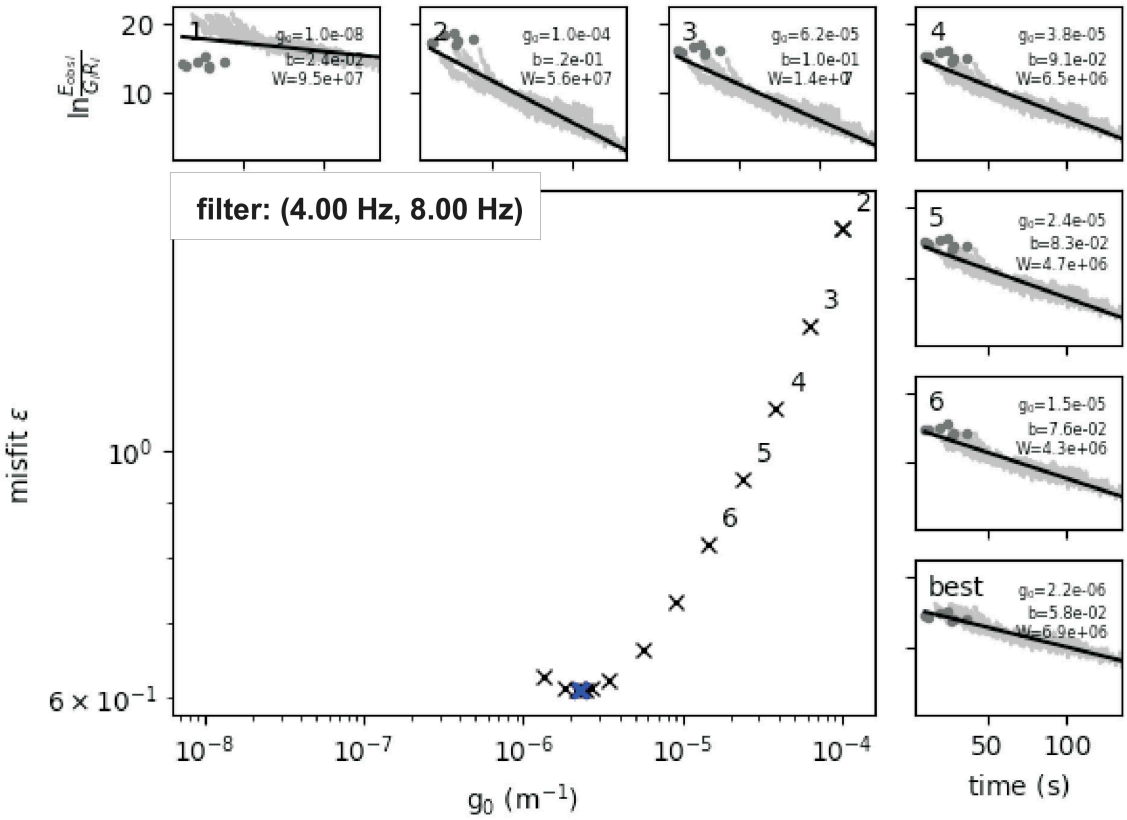

Figure 3.

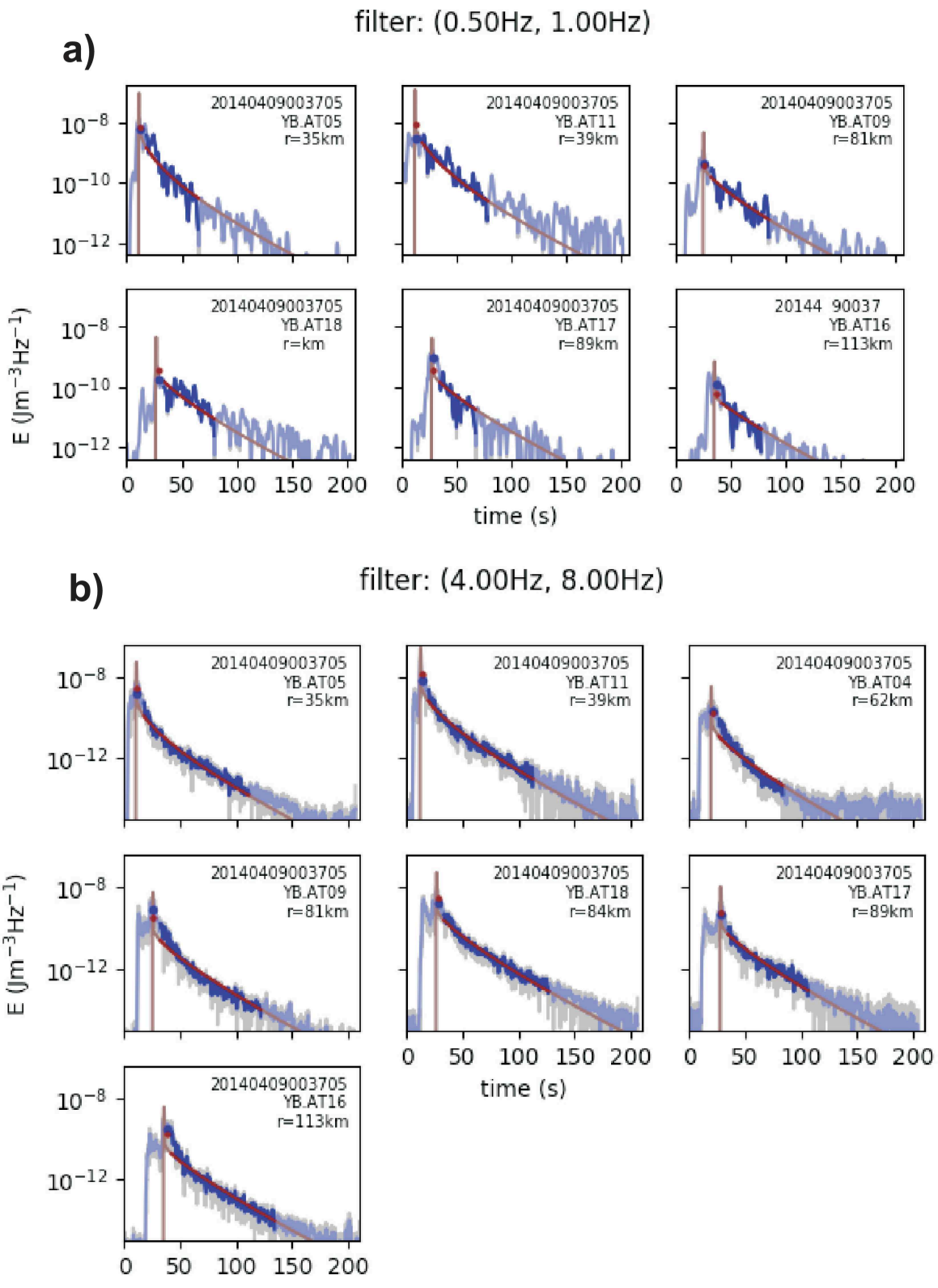
a)
filter: (0.50Hz, 1.00Hz)
20140409003705
YB.AT05
r=35km
20140409003705
YB.AT11
r=39km
20140409003705
YB.AT09
r=81km
20140409003705
YB.AT18
r=km
20140409003705
YB.AT17
r=89km
20144 90037
YB.AT16
r=113km
E (Jm⁻³Hz⁻¹)
time (s)
b)
filter: (4.00Hz, 8.00Hz)
20140409003705
YB.AT05
r=35km
20140409003705
YB.AT11
r=39km
20140409003705
YB.AT04
r=62km
20140409003705
YB.AT09
r=81km
20140409003705
YB.AT18
r=84km
20140409003705
YB.AT17
r=89km
20140409003705
YB.AT16
r=113km
E (Jm⁻³Hz⁻¹)
time (s)

Figure 4.

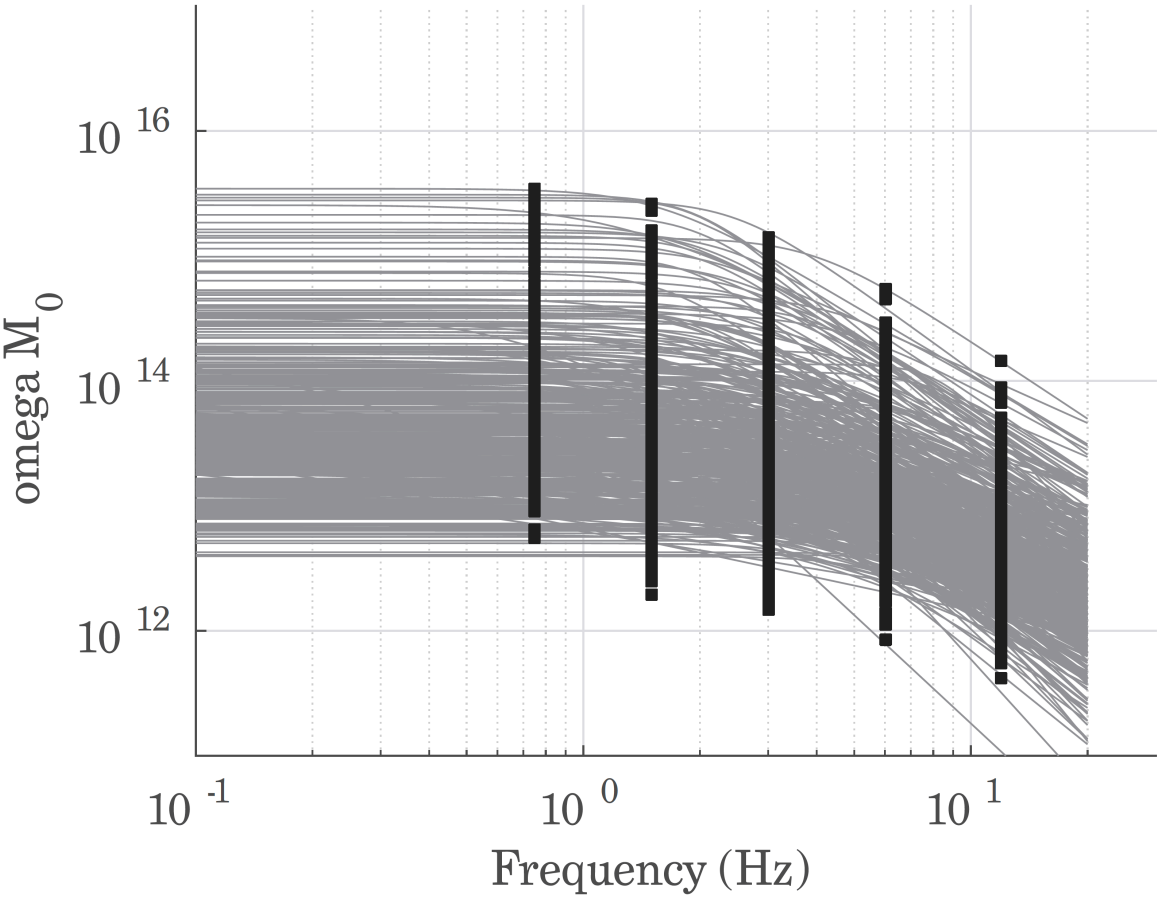

Figure 5.

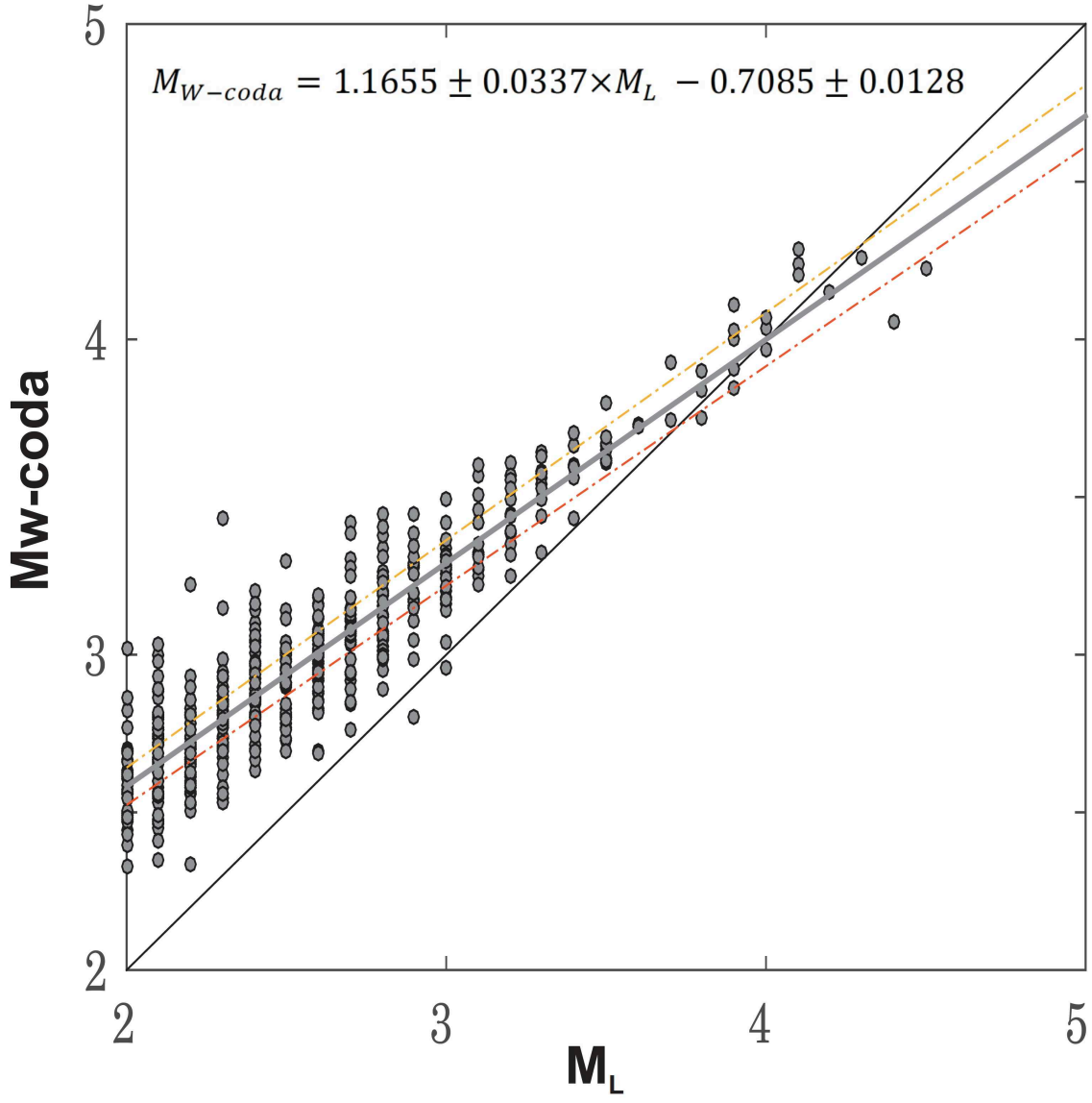

Figure 6.

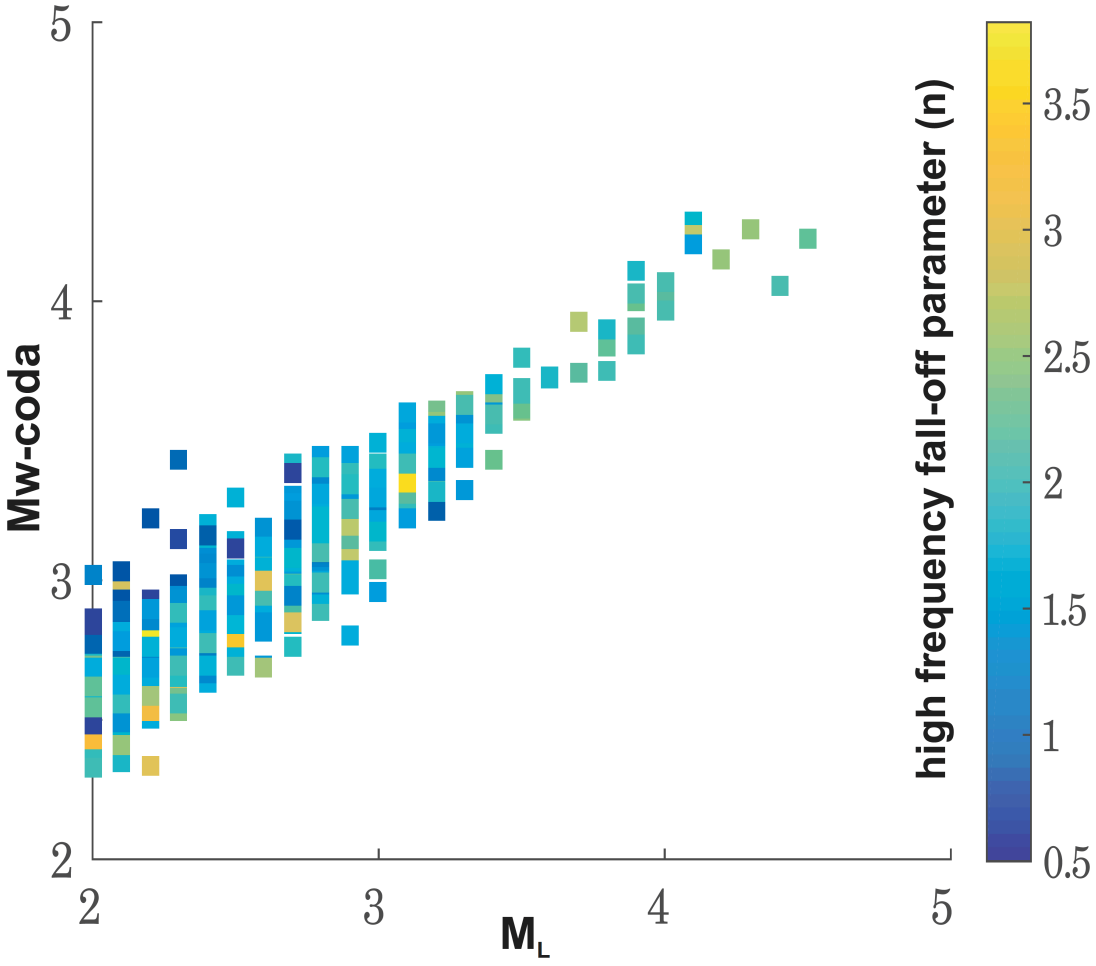
Mw-coda
M_L
high frequency fall-off parameter (n)
5
4
3
2
2
3
4
5
3.5
3
2.5
2
1.5
1
0.5

Figure 7.